Chapter 5 – Results and discussion

This chapter presents and describes the results of the simulations that have been done for the different STHE configurations. It has the following structure:

- Verification
    - Mesh independence study
    - Wall y^+
    - Input verification
- Steady-state simulations
    - Flow paths
    - Pressure drop
    - Bypass flow velocities
    - Baffle-cut velocity
    - Velocity range volume percentage
    - Flow fractions
- Single_60 vs. Single_90
    - High velocity range volume percentage
    - Baffle velocities
    - Symmetry plane flow distribution
- Transient multiphase simulations
    - Symmetry plane sediment concentration
    - Cross-sectional sediment concentration

Two sets of simulations were conducted: steady-state flow simulations of six heat exchangers, and transient multiphase simulations of the baseline and best performing configuration.

The results consist of pressure, velocity and mass flow measurements in specific areas of every heat exchanger and were compared in order to determine the most effective configuration.

A detailed comparison between the Single_60 and best performing configuration follows, discussing and highlighting important differences in more detail. The results of the multiphase simulations conclude the chapter, demonstrating the sediment transport and deposition areas.

5.1. Verification

The following section describes the method of verification and the results that have been obtained.

5.1.1. Mesh independence study

The mesh independence of the simulations will be proven below through refined grid sizes. This is solely to exclude the possibility of mesh influence on the accuracy of the results. The independence study was performed on the Single_61 configuration by measuring the pressure drop over the model. Independence was considered successful if the value thereof did not change noticeably between successive grids.

Steady-state simulations

A set of six simulations were evaluated, each having an increasing number of computational cells, to examine the behaviour of the converged pressure drop values. Table 10 gives the values of the four meshing parameters that were discussed in Chapter 4.1.2, as well as the total number of cells and pressure drop for each simulation. Values in parenthesis are the actual dimensions in millimetres.

Simulation	Base Size	Prism layer thickness	Relative minimum size	Relative target size	Total number of cells	Pressure drop (kPa)
1	40 mm	2.5% (1)	40% (16)	100% (40)	749837	5.699
2	20 mm	5% (1)	40% (8)	100% (20)	2154792	8.786
3	20 mm	5% (1)	30% (6)	100% (20)	2918746	8.314
4	12 mm	5% (0.6)	40% (4.8)	100% (12)	4885949	7.283
5	15 mm	5% (0.75)	40% (6)	100% (15)	5894761	7.981
Final	10 mm	10% (1)	40% (4)	100% (10)	9369395	7.594

Table 10: Results of steady-state mesh independence study

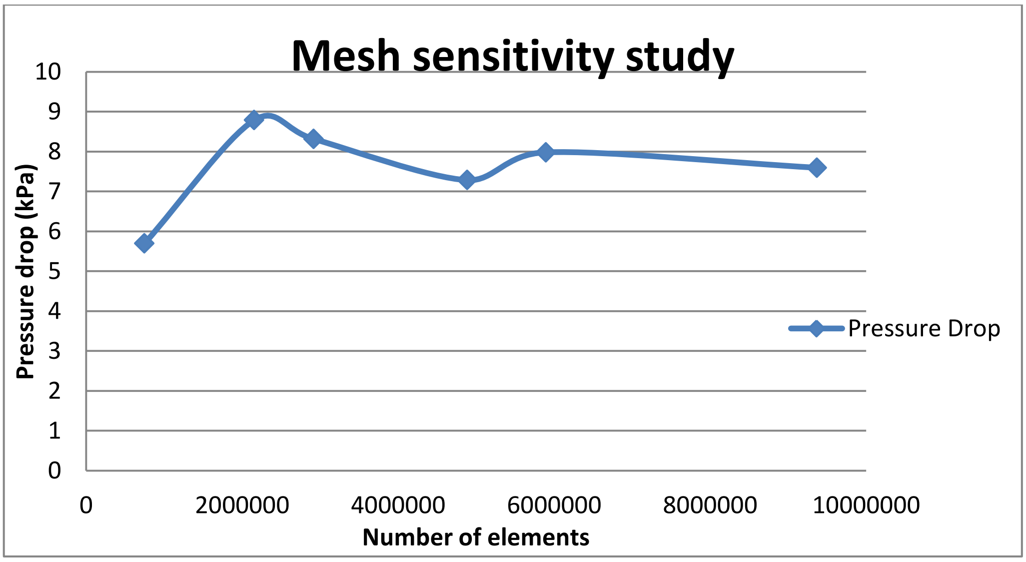

Figure 35: Graph of steady-state mesh sensitivity study for pressure drop vs. mesh size

The results shown in Figure 35 indicate that the final grid resolution is sufficient (Table 10). The pressure drop is shown to converge, confirming that mesh independence has been achieved. This conclusion is drawn from the slope of the curve in Figure 35, in other words the change in pressure drop is slight if compared to the large increase in number of elements. The preceding points tend to oscillate around a central value, finally attaining convergence just below a value of 8 kPa. A similar oscillation is also observed in all the simulations discussed below.

Transient multiphase simulations

The results tabulated and depicted below are of the mesh independence study for the transient multiphase simulations (Chapter 4.2). Once again, the values of the four important mesh parameters were varied in order to obtain different mesh sizes. The simulations were conducted for the altered Single_60 configuration.

Simulation	Base size	Prism layer thickness	Relative minimum size	Relative target size	Total number of cells	Pressure drop (kPa)
1	50 mm	16% (8)	40% (20)	250% (120)	508057	9.780
2	40 mm	20% (8)	40% (16)	250% (100)	785953	10.526
3	30 mm	33% (10)	50% (15)	250% (75)	853773	10.470
4	30 mm	20% (6)	34% (10.2)	250% (75)	1135974	11.155
5	25 mm	24% (6)	40% (10)	200% (50)	1988564	11.085
Final	25mm	24% (6)	34% (8.5)	250% (62.5)	2973626	11.164

Table 11: Mesh independence study of the transient multiphase simulations

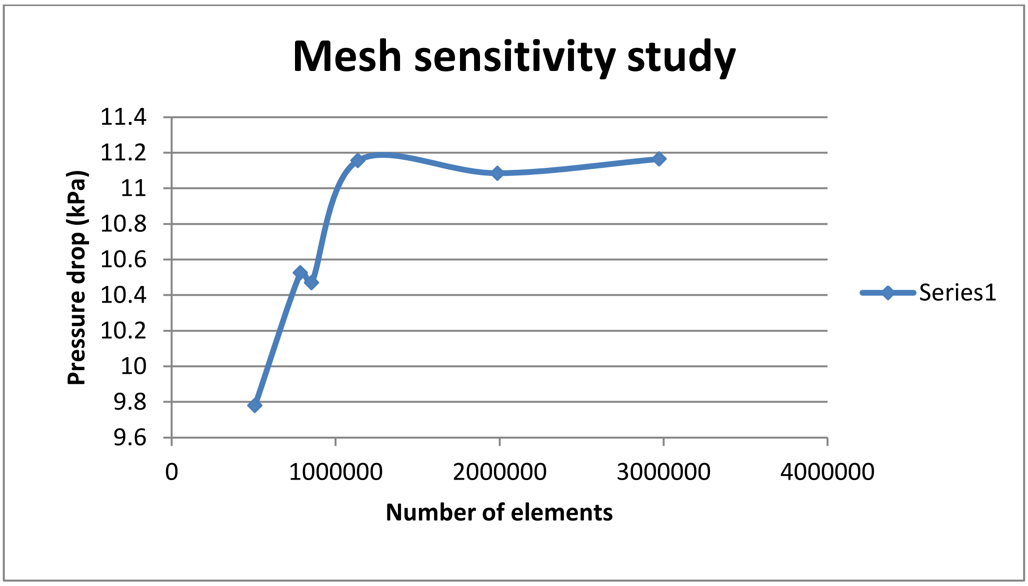

Figure 36: Graph of transient multiphase mesh sensitivity study for pressure drop vs. mesh size

The results shown in Table 11 also show that mesh independence had been reached. This ensures that the simulations will run stable and accurate results can be obtained.

5.1.2. Wall y+

As discussed in Chapter 3.5, the software deals with boundary layer flow in a different manner than in free stream flow. In order to validate that the use of a turbulence model is correct and that the generated mesh is sufficiently fine for the specific flow conditions, the wall y^+ values of the realizable k-ε model have to be less than 300, above which validity and accuracy decreases (STAR-CCM+ User Guide v.6.06, 2011:2357).

Steady-state simulations

The wall y^+ maxima of the 18 simulations that were conducted are presented in Table 12.

Maximum wall Y^+ values for different sections of configurations					
Single_61	78.712	Double_61	82.305	DnD_61	66.642
Single_62	73.642	Double_62	95.152	DnD_62	72.505
Single_63	53.887	Double_63	115.363	DnD_63	82.918
Single_91	56.969	Double_91	55.185	DnD_91	73.630
Single_92	52.903	Double_92	84.155	DnD_92	107.942
Single_93	81.388	Double_93	89.147	DnD_93	83.850

Table 12: Wall y^+ maxima for six configurations

All y^+ values that are shown above are within the required range; thus the boundary layer mesh resolution is sufficiently fine for the turbulence model that is used.

Transient multiphase simulations

The wall y^+ maxima of the transient multiphase simulations are 268.36 and 220.78 for the modified Single_60 and Single_90 simulations, respectively, also indicating that the transient multiphase mesh resolution is sufficient.

5.1.3. Input verification

STAR-CCM+ is a validated, commercial CFD software package. According to De Wet (2011), the package has been validated against numerous studies of DNS and experimental results, and can therefore satisfactorily solve the mentioned flow phenomena.

In order to verify whether the present results are valid (due to the absence of explicit experimental data), the inputs to the package have to be scrutinized. This will be achieved by simulating and replicating the results of an experimental study on sedimentation tanks by applying the same solution methodology that was used in the transient multiphase simulations. Details of the work done by Van Antwerpen (2000) that are relevant to the present study are presented below.

Van Antwerpen (2000) studied effects of sediment tank configuration on the settling characteristics within to establish methods for design and improve numerical modelling of sedimentation tanks. It was mainly aimed at assisting engineers and plant managers in designing tanks optimally and attaining operational parameters that reduce energy consumption.

Two parameters were used for the validation procedure, namely, the paths of the particles and area of build up. Information on the concentration of sediment at deposition areas and sedimentation rate were unfortunately unavailable.

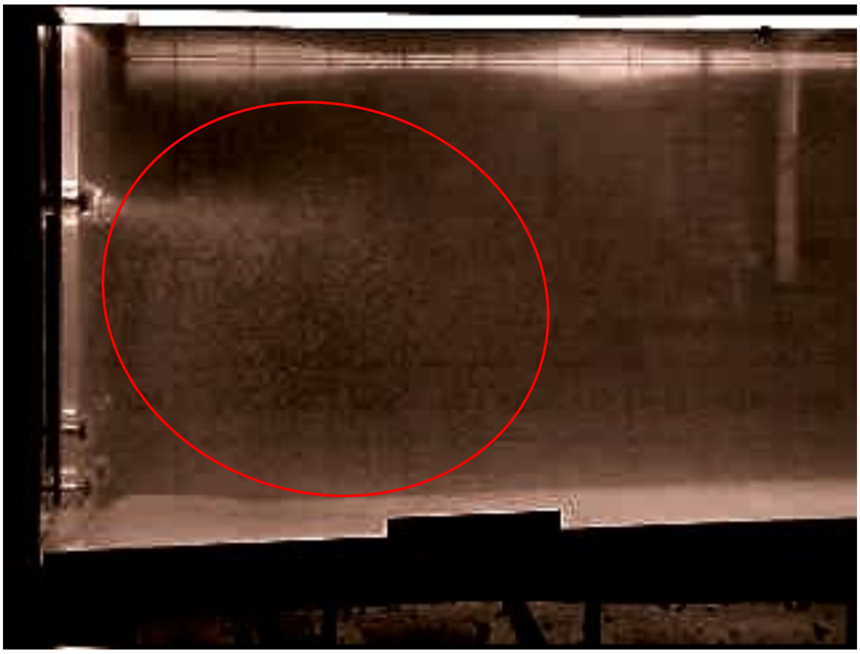

Figure 37: Experimental results of particle distribution (Van Antwerpen, 2000)

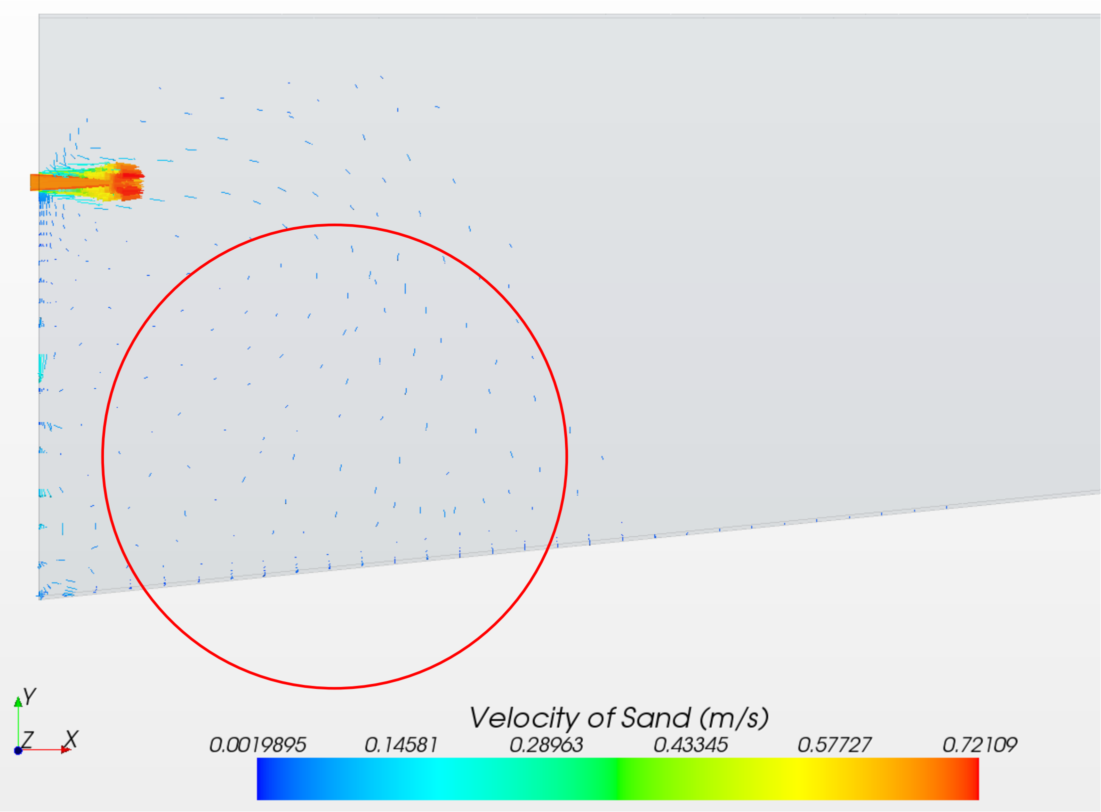

Figure 38: Numerical results of sedimentation tanks for particle paths

In Figure 37 the inlet and bottom section of the experimental sedimentation tank is shown. Although not entirely clear, the cloudiness of the particles in suspension is visible as a colour deviation. The visible areas of suspension reveal the underlying velocity fields and are reflected in the numerical simulation (Figure 38). By comparing these figures, the distribution of particles can be seen to be similar. This is an indication that the effect of velocity on the phase-interaction and particle distribution is accurate.

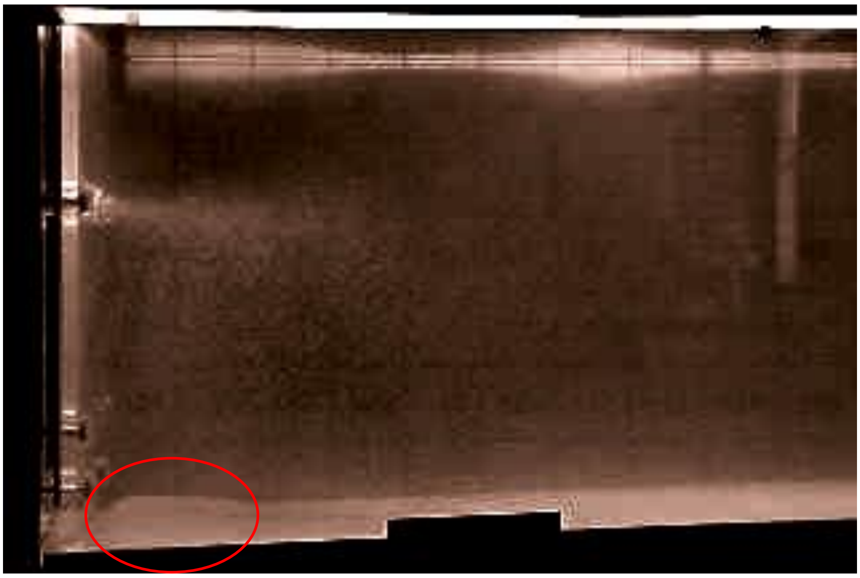

Figure 39: Experimental results of particle deposition (Van Antwerpen, 2000)

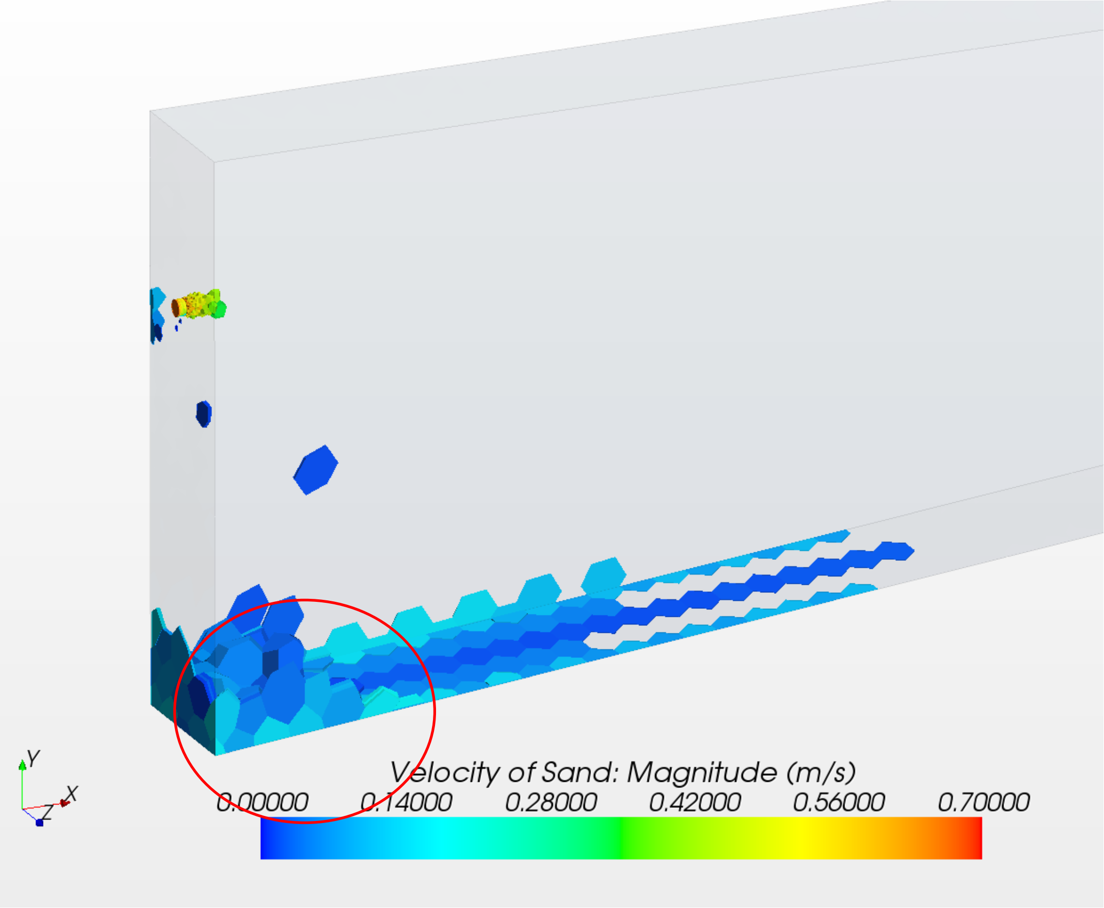

Figure 40: Isometric view of numerical simulation of particle deposition

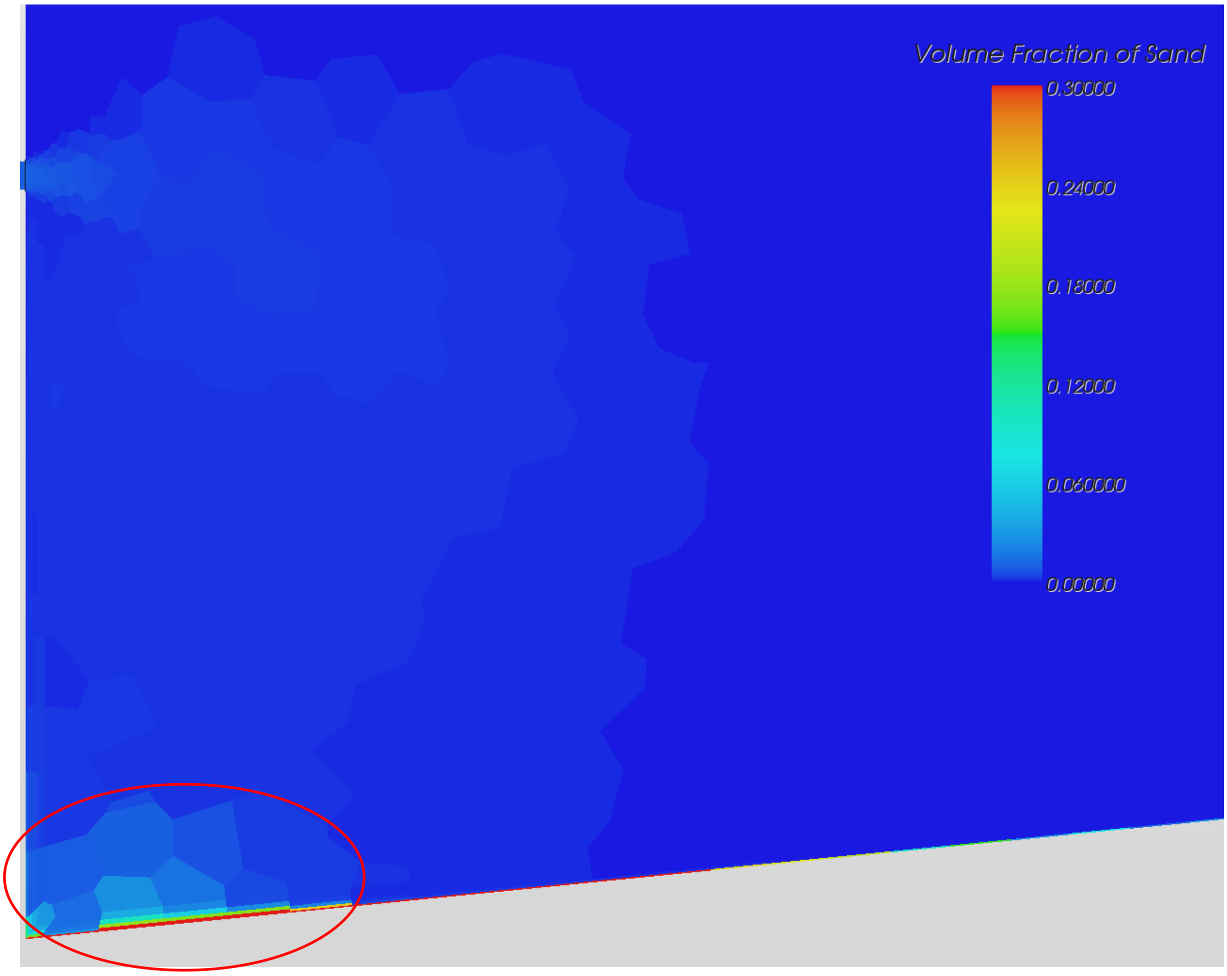

Figure 41: Numerical result of particle deposition and concentration on the tank surface

Figure 39 shows the area of deposition of sediment at the bottom of the sedimentation tank, close to the rearward boundary. This deposition is once again reflected in Figure 40 and Figure 41, where the latter also gives an indication of the particle paths previously discussed. From the images depicting particle distribution, a similar conclusion can be drawn. Areas of particle deposition in the numerical and experimental results are shown to have a similar arrangement. In Figure 41, there is a build-up of particles at the same distance from the rearward edge (at roughly 40 mm), which is also highlighted in Figure 39. This deposition has a similar shape as that depicted in Figure 39 and can be seen in greater detail in Figure 42 below.

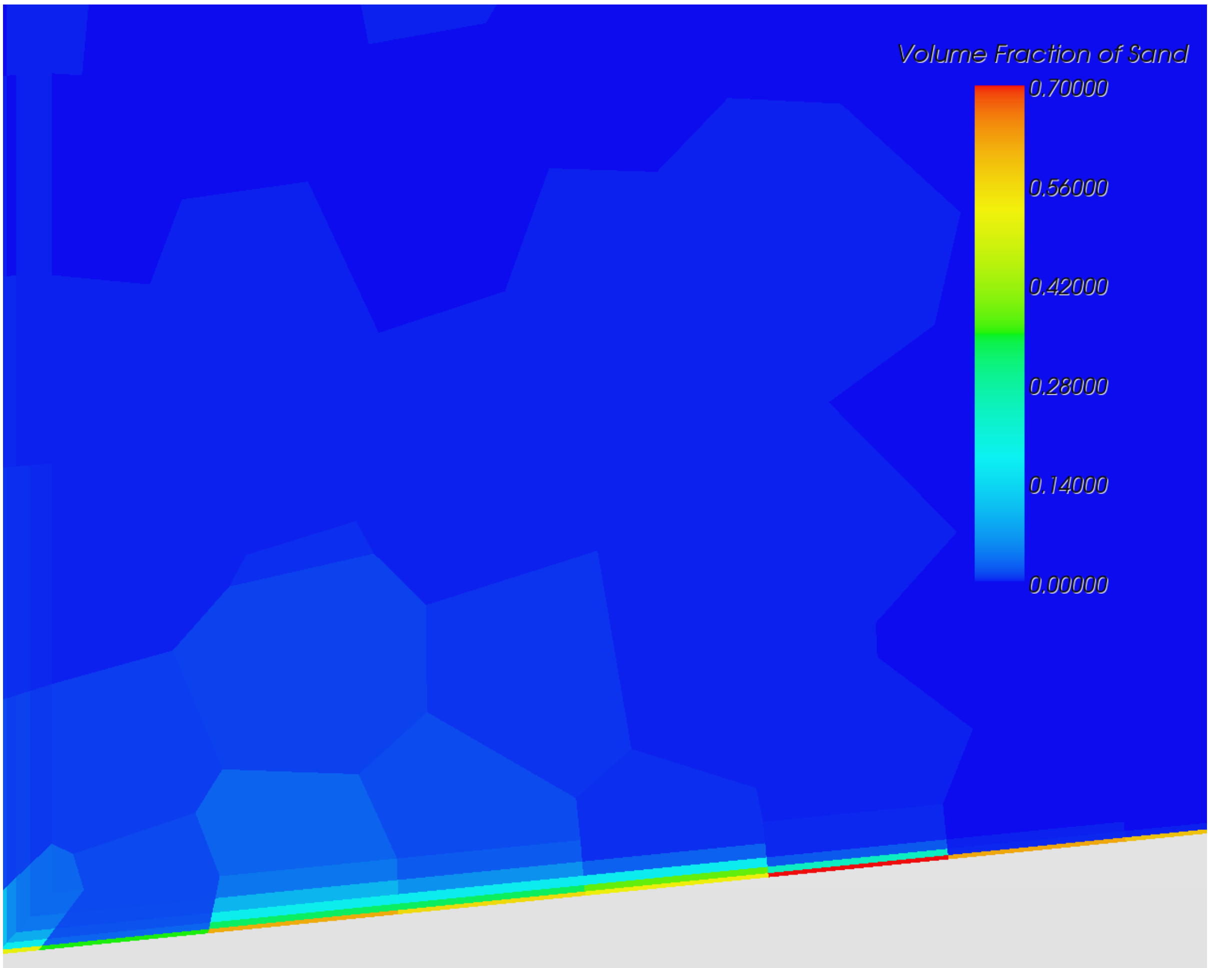

Figure 42: Detail view of sediment concentration

From the results presented above, it can be expected that the sediment deposition would continue to increase in the bottom left corner of the sedimentation tank, progressing upward and to the right. This will continue for a considerable time, until deposition-transportation equilibrium has been reached and the sediment transported through the outlet.

A second important conclusion from the numerical results is that the simulation of transient multiphase flows can be done successfully. Transient multiphase simulations are prone to instability, especially due to areas of high particulate concentrations. The present simulation was shown to be stable for cells having cell-dispersed phase fractions in excess of 50%.

It can be concluded from the results above that the software can adequately simulate transient multiphase flows, albeit cumbersome. Particle paths, distributions and deposition were accurately simulated and correlated well with visual experimental results.

5.2. Steady-state simulations

5.2.1. Flow paths

In Figure 43 to Figure 48, images of the symmetry plane flow paths for the single-segmental, double-segmental and disc-and-doughnut configurations are presented in order to illustrate and compare the general velocity distribution in the configurations visually.

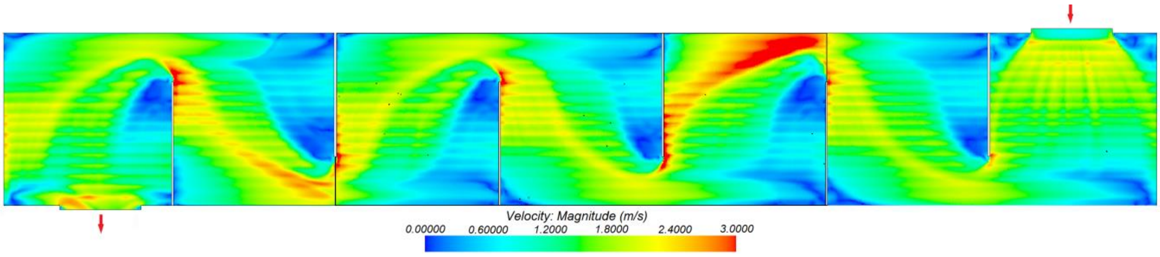

Figure 43: Flow path on the symmetry plane of the Single_60 configuration

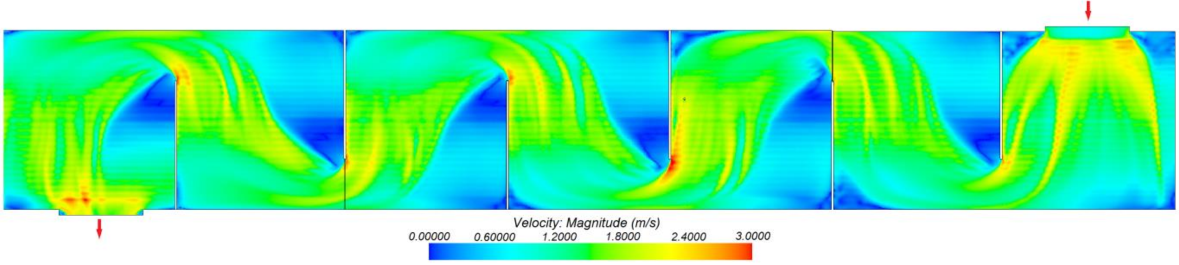

Figure 44: Flow path on the symmetry plane of the Single_90 configuration

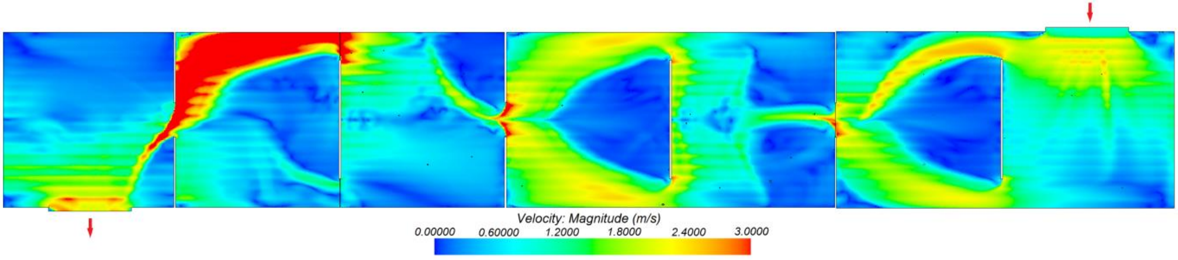

Figure 45: Flow path on the symmetry plane of the Double_60 configuration

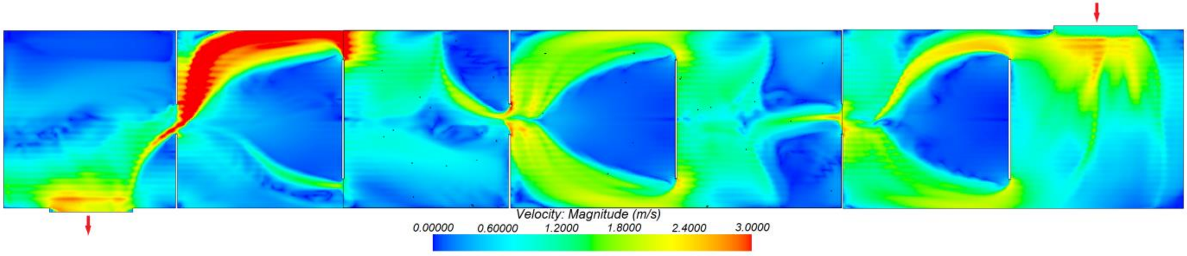

Figure 46: Flow path on the symmetry plane of the Double_90 configuration

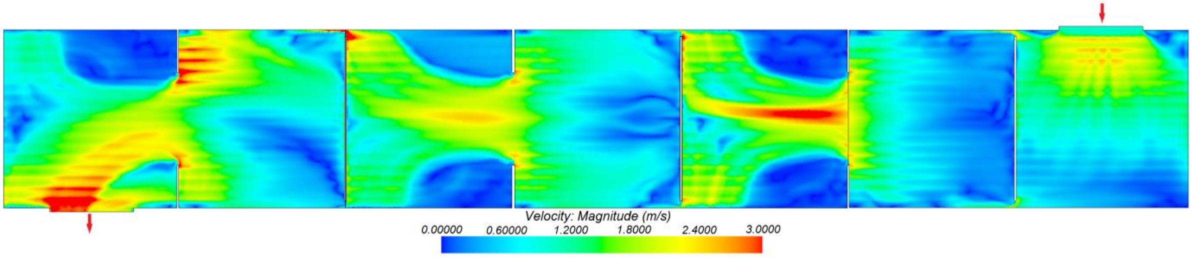

Figure 47: Flow path on the symmetry plane of the DnD_60 configuration

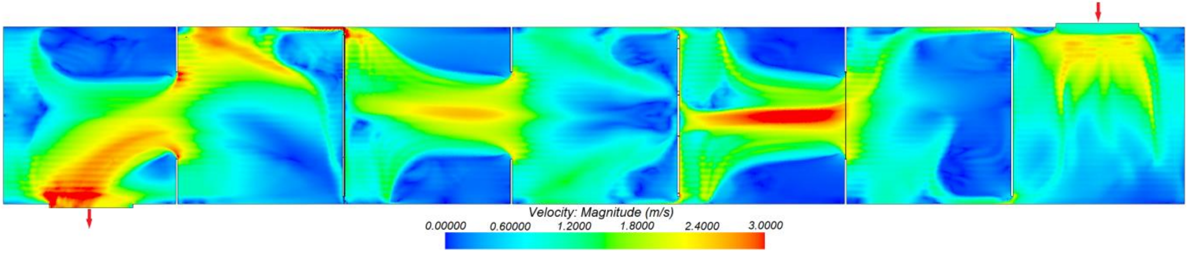

Figure 48: Flow path on the symmetry plane of the DnD_90 configuration

The figures above give an indication of the outcomes to be expected. The single-segmental configurations, especially the rotated triangular configuration (Figure 43 and Figure 44), have the largest pass-partition flow velocities. Figure 43 can be seen to have the large areas of colours indicating intermediate velocities (1.8 m/s to 2.4 m/s) which are not as prominent in the other configurations and is also confirmed by Shilling (1997:33). Figure 44 shows that the Single_90 configuration behaves in similar fashion, giving rise to the possibility that it is a viable alternative. The configuration has a decent velocity distribution and smaller recirculation regions with higher velocities behind baffles, when compared to the disc-and-doughnut and double-segmental configurations.

The remaining configurations (Figure 45 to Figure 48) show larger areas of low velocity flow, specifically in the recirculation regions behind baffles. This difficulty is further complicated by the fact that the models are symmetric not only about a vertical plane, but also about a horizontal plane. The size and volume of the recirculation areas are thus increased, which inevitably increases the probability of an increased sedimentation rate.

A second important characteristic observed in the recirculation zones is the difference in turbulence structures between the rotated triangular and square tube configurations. These differences are clearly visible in the third compartment of Figure 47 and Figure 48. The characteristics are important indicators of heat transfer efficiency and velocity distributions.

From Figure 45 and Figure 46, it can be argued that the double-segmental configurations have high velocities, but most of the areas where this higher velocity flow is concentrated is in regions where the flow is longitudinally or diagonally oriented. This renders these regions ineffective when compared with the single-segmental configurations. Though not as prominent, similar conditions exist in the disc-and-doughnut configurations.

A second characteristic of the disc-and-doughnut and double-segmental configurations is that the regions of the configurations that do exhibit cross-flow are much smaller than that of the single-segmental configurations. This once again places the single-segmental configurations in a favourable light.

Vector plots of the cross-flow distribution in the sixth compartment (at five planes, each spaced 200 mm apart) are available in Appendix D. It gives an indication of the flow paths within the bundles

5.2.2. Pressure drop

The total pressure drop of the six configurations is presented in Table 13:

	Total	Percentage Difference
S6	30.89	-
S9	28.95	93.73%
D6	24.29	78.64%
D9	22.99	74.44%
DD6	22.70	73.49%
DD9	23.91	77.40%

Table 13: Total pressure drop for the six configurations

If one considers the discussion on heat exchanger pressure drop in Chapter 2.3, the results of the pressure drop for the six configurations in Table 13 are to be expected. The disc-and-doughnut configurations have the lowest pressure drop, followed by the double-segmental and single-segmental configurations. This dissimilarity can be attributed to the reduced number of major restrictions encountered by the flow, as compared with the single-segmental configurations. The percentage difference of the models measured from the base case is tabulated in the last column.

The results for total pressure vary somewhat to the evidence that is found in literature. The disc-and-doughnut configurations could have a pressure drop of up to 55% less than the single-segmental configurations (Li and Kottke, 1999:3521; Donohue, 1949:2511). The variation can be attributed to the difference in geometry. The heat exchangers simulated in the present study have a larger number of major restrictions and reduced flow area within the bundle which can be attributed to the 20% increase in expected pressure drop.

With exception of the disc-and-doughnut configurations, the pressure drop for rotated triangular tube configurations is higher than for the square arrangement, which is in line with the results of Iwaki *et al.* (2004:363) and Khan *et al.* (2006:4838).

The results of the calculations that were presented by Gaddis and Gnielinski (1997:154) as well as Kapale and Chand (2006:607) for the Single_60 configuration are available in Appendix B and are tabulated in Table 14. These procedures have been discussed superficially and briefly in Chapter 3.6.

Correlation pressure drop [kPa]			
	G&G	K&C	Simulated
Single_60	33.25	34.27	33.89
Single_90	27.84	29.95	28.95

Table 14: Results of pressure drop predicted by correlations

The results from the simulations are in good agreement with the correlations of Gaddis and Gnielinski (1997:154) as well as Kapale and Chand (2006:607). The pressure drop of square and rotated triangular tube arrangements for single-segmental baffled heat exchangers was calculated and was within 4.0% for the first correlation and within -3.3% for the second. The values for square tube layout were closer to the correlations than the rotated triangular arrangements. The error percentage for the correlation of Gaddis and Gnielinski (1997:154) is between 28.0% and 1.5% of experimental results and the present results fall well within this margin. Similarly, the correlation of Kapale and Chand (2006:607) has an error range of between 2.4% and -4.0% of experimental results and the present results fall within this margin.

5.2.3. Bypass flow velocities

Maximum and average flow velocities in the bundle-shell and pass-partition bypass regions were evaluated and are tabulated in Table 15 through Table 18. A small difference between maximum and average bypass velocities in relation to the cross-flow maximum and average velocities will indicate that a larger flow percentage will inevitably not bypass the bundle, but penetrate it, resulting in higher cross-flow, mass flow fractions. Configurations with lower values are deemed to have better bypass performance.

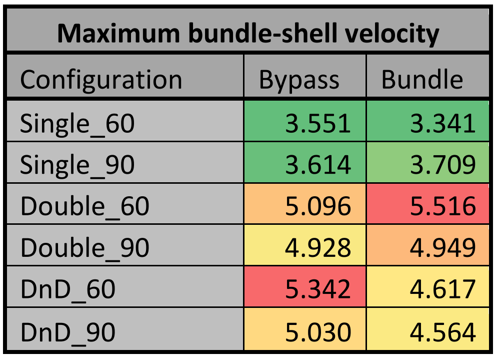

Maximum bundle-shell velocity		
Configuration	Bypass	Bundle
Single_60	3.551	3.341
Single_90	3.614	3.709
Double_60	5.096	5.516
Double_90	4.928	4.949
DnD_60	5.342	4.617
DnD_90	5.030	4.564

Table 15: Maximum bundle-shell bypass velocity

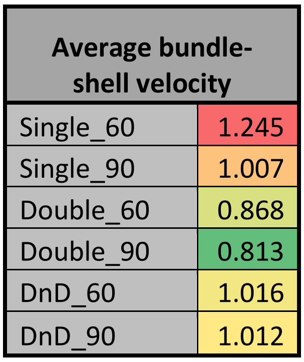

Average bundle-shell velocity	
Single_60	1.245
Single_90	1.007
Double_60	0.868
Double_90	0.813
DnD_60	1.016
DnD_90	1.012

Table 17: Average bundle-shell bypass velocity

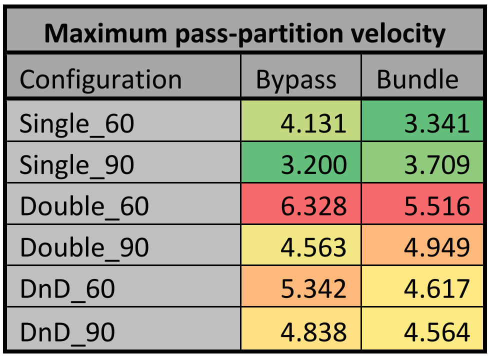

Maximum pass-partition velocity		
Configuration	Bypass	Bundle
Single_60	4.131	3.341
Single_90	3.200	3.709
Double_60	6.328	5.516
Double_90	4.563	4.949
DnD_60	5.342	4.617
DnD_90	4.838	4.564

Table 16: Maximum pass-partition bypass velocity

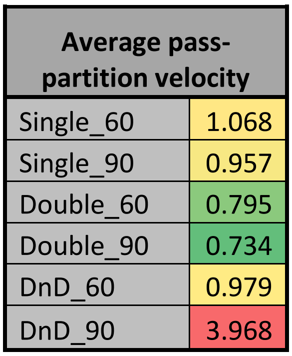

Average pass-partition velocity	
Single_60	1.068
Single_90	0.957
Double_60	0.795
Double_90	0.734
DnD_60	0.979
DnD_90	3.968

Table 18: Average pass-partition bypass velocity

All configurations performed consistently with regard to the difference between bundle and bypass maxima (Table 15 and Table 16), except the maxima values of the double-segmental configurations in which the bundle bypass velocities are higher than the bypass. For both bypass streams, the base model had the lowest peak velocities with higher average bypass velocities. The base case configuration had the highest average bypass velocities (Table 17 and Table 18) with slight differences between bypass and bundle velocities. The Double_90 configuration has overall best performance considering average velocities, bundle-bypass differences and has lower-mid-range peak values, making it the best performing model, when examining bypass flows. The values that are presented in Table 15 to Table 18 were calculated for a constant bypass volume.

The trends that were observed for the bypass flow measurements are to be expected. The flow in double-segmental and disc-and-doughnut configurations with the square tube arrangement experiences less resistance. This results in less flow being diverted into the bypass streams and can be seen in the fraction measurements for cross-flow, discussed later in this chapter.

The maxima of the double-segmental and disc-and-doughnut configurations are situated in larger areas of the bypass regions at the top of the exchanger, which results in effective heat transfer. This large concentration of high velocity flow is counteracted by a drastic reduction of the velocity at the bottom of the heat exchanger which will be detrimental to the sedimentation transport characteristics of the configurations.

It has to be reiterated that bypass streams are less effective at heat transfer than the preferred cross-flow. Although the Double_60 configuration has the highest bundle velocity and lowest average bypass values, the flow is more longitudinally oriented than perpendicular.

5.2.4. Baffle-cut velocity

Maximum and average flow velocities through the baffle-cut regions were evaluated and are tabulated below. Because of limited velocities at the inlet conditions, high baffle-cut velocities are crucial for sediment transport and improved heat transfer throughout the heat exchanger.

Average baffle-cut velocity (m/s)						
	Baffle 1	Baffle 2	Baffle 3	Baffle 4	Baffle 5	Baffle 6
Single_60	1.796	1.982	1.852	1.894	1.940	1.876
Single_90	1.683	1.798	1.714	1.723	1.742	1.728
Double_60	1.767	1.999	1.913	1.924	1.975	2.029
Double_90	1.757	1.879	1.828	1.799	1.920	1.841
DnD_60	1.727	1.838	1.913	1.924	1.905	1.798
DnD_90	1.751	1.875	1.747	1.782	1.905	1.823

Table 19: Average baffle-cut velocity

Maximum baffle-cut velocity (m/s)						
	Baffle 1	Baffle 2	Baffle 3	Baffle 4	Baffle 5	Baffle 6
Single_60	2.720	2.940	3.298	3.282	3.070	3.337
Single_90	2.624	2.559	3.022	2.886	2.690	2.758
Double_60	2.617	3.311	2.997	3.283	4.480	5.162
Double_90	2.406	2.566	2.828	2.893	4.063	3.060
DnD_60	2.397	2.501	2.307	2.586	5.113	3.122
DnD_90	2.651	2.510	2.270	2.473	4.621	2.930

Table 20: Maximum baffle-cut velocity

The square configurations generally have the highest average and maximum baffle-cut velocities, which is to be expected because of the increased number of major restrictions. The Double_60 configuration has the highest average and maximum baffle-cut velocity for most of the baffle-cut planes. The base configuration is not far off for both average and maximum velocities. The minimum average and maximum velocity falls to the Single-90 and DnD_90 configurations respectively.

For all configurations, the average velocity tends to stay relatively constant, facilitating mass conservation. The minor discrepancies observed are due to the non-zero residuals of the continuity equation.

Overall, the velocities in the baffle windows are the highest. The sizes of these regions can be compared by examining the figures in Appendix H for velocities larger than 2 m/s. It can be observed that the single-segmental configurations have the smallest concentration of flow with velocity larger than 2 m/s. Attention is once again directed towards the large concentration of velocity at the top of the end of the double-segmental and disc-and-doughnut configurations, as well as the lack thereof at the bottom.

It might seem that the maxima for the disc-and-doughnut and double-segmental configurations are erroneously high. When taking the visual results in Appendix E and

Appendix H into account, it can be seen that a large portion of the flow is diverted into the bundle-bypass stream resulting in inefficient flow. The average velocity over the baffles is still similar in magnitude, indicating that continuity is conserved.

The baffle-cut velocity results clearly indicate that the Single_60 and Double_60 configurations are dominant.

5.2.5. Velocity range volume percentage

Threshold is a function that is built into STAR-CCM+; it enables the user to specify and select cells within, above or below a certain range for specific criteria (for instance, all cells with velocities larger than 0.5 m/s) and it applies a function/representation to the selection. Consequently, this function has been used to identify the cells that have velocities falling within certain ranges. The specified velocity ranges are the following: smaller than 0.05 m/s, between 0.05 and 0.1 m/s, 0.1 and 0.15 m/s, 0.15 and 0.2 m/s, 0.2 and 0.25 m/s, 0.25 and 0.5 m/s and larger than 0.5 m/s (Figure 49). The volumes of the highlighted cells were computed, yielding the ability to compare low-flow velocity zones in the configurations. Results that are tabulated in Table 21 are presented as fractions of the total configuration volume.

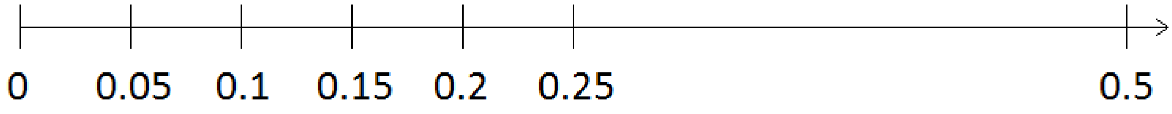

Figure 49: Line diagram of the threshold velocity ranges in m/s

The goal of these results is to give an indication of where the majority of the flow is concentrated within the heat exchanger and tube bundle, respectively. The differentiation between the heat exchanger and tube bundle is made to illustrate the effect and prominence of the bypass streams as well as the potential of the cross-flow stream. For this reason, the threshold velocity range occurs twice within the table for full volume and main cross-flow measurements, respectively. In other words, the table below shows row headings for two cases of a single velocity threshold. The first rows are the threshold distribution without any exclusion. Thus, the bundle bypass and pass-partition lane flows are included in the result (streams C and F in Figure 7). The second rows show the result for velocity threshold with the streams excluded. This singles out the main cross-flow velocity in each heat exchanger (Figure 50).

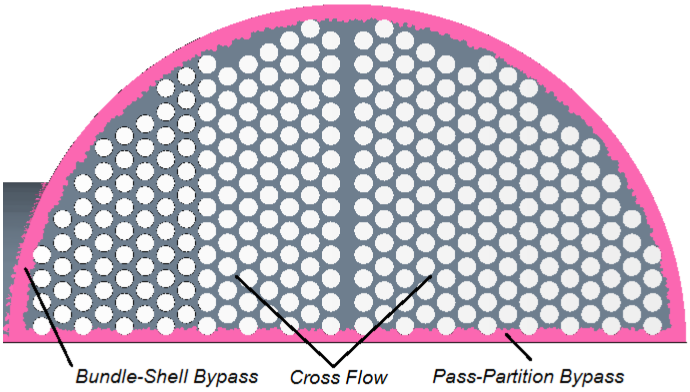

Figure 50: Bypass streams

The most effective configuration will be selected mainly from the results in Table 21 with consideration given to other discussions, based on where or in what range the most effective flow is concentrated. Thus, the configuration with limited low-velocity and greater high-velocity concentrations would be favoured.

Total percentage of volume of cells within specified velocity range						
Range	Single_60	Single_90	Double_60	Double_90	DnD_60	DnD_90
V < 0.05	0.690	1.047	8.169	7.449	4.767	6.743
V < 0.05	0.661	0.932	7.614	6.915	4.317	6.002
0.05 < V < 0.1	2.417	3.638	12.190	12.249	8.038	9.832
0.05 < V < 0.1	2.303	3.421	11.076	11.105	7.455	9.012
0.1 < V < 0.15	4.351	4.941	9.564	9.623	8.190	8.921
0.1 < V < 0.15	4.164	4.714	8.508	8.710	7.728	8.308
0.15 < V < 0.2	5.930	5.516	7.009	7.308	7.501	7.725
0.15 < V < 0.2	5.718	5.299	6.258	6.552	7.098	7.201
0.2 < V < 0.25	6.789	6.013	5.602	5.857	6.588	6.532
0.2 < V < 0.25	6.591	5.781	4.934	5.174	6.186	6.034
0.25 < V < 0.5	27.891	27.252	17.689	18.630	22.666	21.390
0.25 < V < 0.5	26.618	25.653	15.526	15.874	20.422	18.792
0.5 < V	51.930	51.593	39.775	38.883	42.250	38.856
0.5 < V	38.858	41.717	30.404	30.319	31.892	29.283

Table 21: Total percentage of volume of cells within specified velocity range

The poorest performing model is the DnD_90 configuration, having the lowest high-velocity concentrations, whilst the Double_60 configuration has the highest low-velocity concentration. The best performing model is a close contention between the Single_60 and Single_90 configurations. The models have excellent low-velocity performance and surpass the other configurations on the opposite end of the scale.

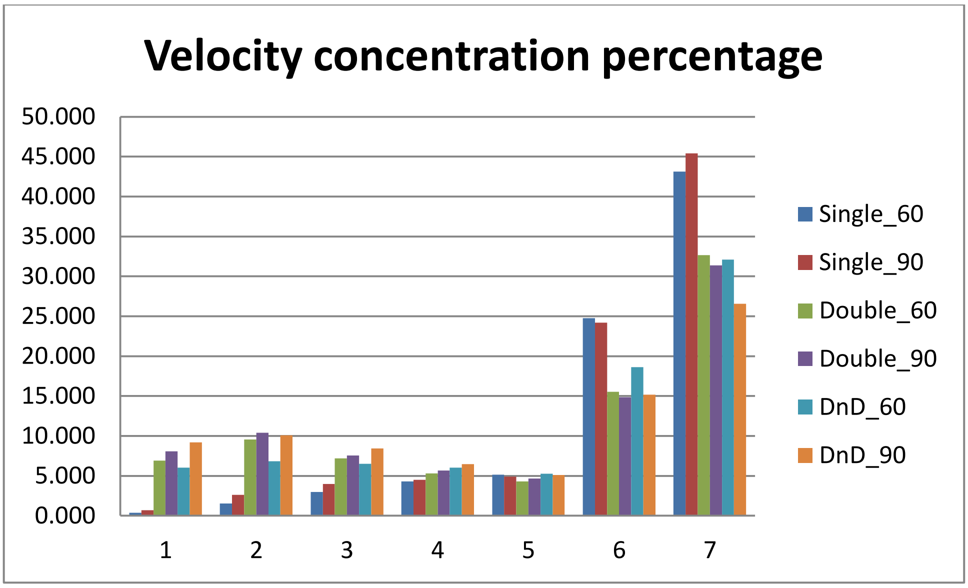

Figure 51: Velocity percentage concentrations for main cross-flow

Figure 51 above is a visual representation of the results Table 21, clearly indicating the dominance of the single-segmental configurations due to their relative position on the lower and upper ends of the velocity scale.

The prominence of the bypass flows are presented in Table 22. The values are calculated from the difference between volumes of the full flow and the main cross-flow. Bypass flows have greater concentrations in the higher flow velocity regions. A configuration is deemed to be effective if less of the bypass flow is concentrated in the higher velocity regions, indicating that the resistance to main cross-flow is minor. The single-segmental configurations performed the best, having the lowest percentage bypass flow, while the Double_60 configuration had the worst performance overall.

Total percentage of volume of cells within specified velocity range						
Range	Single_60	Single_90	Double_60	Double_90	DnD_60	DnD_90
V < 0.05	0.029	0.115	0.556	0.534	0.450	0.742
0.05 < V < 0.1	0.114	0.217	1.114	1.144	0.583	0.820
0.1 < V < 0.15	0.188	0.228	1.057	0.914	0.462	0.612
0.15 < V < 0.2	0.212	0.217	0.751	0.756	0.403	0.524
0.2 < V < 0.25	0.198	0.231	0.668	0.683	0.403	0.498
0.25 < V < 0.5	1.273	1.598	2.163	2.756	2.244	2.598
0.5 < V	13.072	9.875	9.370	8.564	10.358	9.573

Table 22: Bypass stream volume percentages

Even with 13% and 10% of the single-segmental configurations' flow bypassing the tube bundle, the configurations also have higher flow velocities and concentrations in the cross-flow area compared to other configurations. It is also clear that the percentage of bypass flow for the single-segmental configurations is consistently lower at low velocities. This result provides excellent motivation for the transient multiphase modelling of the single-segmental configurations because of the high velocities present in the bundle, which results in effective transportation of sediment whilst satisfying the requirement of heat transfer.

5.2.6. Flow fractions

In Chapter 2, a discussion was presented on the flow streams within an STHE. These streams have been measured in the present simulations and the results thereof are presented in Table 23.

Results have been obtained by measuring the mass flow rate through planes that are perpendicular to the pass-partition, bundle bypass and cross-flow sections of the heat exchanger, representing Stream F, Stream C and Stream B. The planes are positioned to provide 100% mass flow coverage – all the flow will cross the plane (Figure 52). The planes are positioned in the second, fourth and sixth compartments of each heat exchanger. The mass flow over the outlet of the compartment is also measured in order to determine the accuracy of the calculated flow fractions.

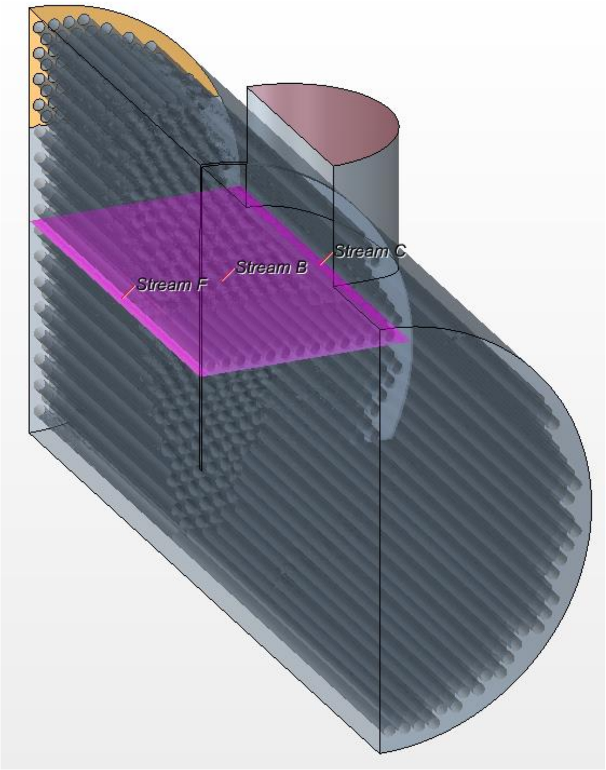

Figure 52: Mass flow plane

If one considers the circular plane that is constructed in the disc-and-doughnut configurations, it is clear that due to the circular construction of the configuration, the effect of bundle-shell bypass flow is negated, generating higher cross-flow fractions.

	Cross-flow (Stream B)	Bundle-shell (Stream C)	Pass-partition (stream F)
Single_60	57.2%	26.7%	16.1%
Single_90	64.1%	21.8%	14.0%
Double_60	61.2%	24.9%	13.9%
Double_90	73.3%	15.2%	11.5%
DnD_60	85.2%	0%	14.8%
DnD_90	90.3%	0%	9.7%

Table 23: Flow fractions for the six heat exchanger configurations

The results in Table 23 are in disagreement with the values that are given in Chapter 3 by Lombaard (2011) in Table 1. For a single-segmental configuration, the cross-flow stream was over predicted by 23.5%, and the bundle-shell and pass-partition streams were underpredicted by 20.9% and 16.1%, respectively. In the present study, streams A and E have still to be taken into account, which could influence the flow fractions by up to 30% (Li and Kottke, 1998b:433).

The results are, however, in better agreement with the results of Palen and Taborek (cited by Mohammadi, 2011) in Table 2. The cross-flow and bundle bypass fractions fall within the given range, with the pass-partition stream that is unaccounted for.

The values in Table 23 give insight into why the double-segmental and especially disc-and-doughnut configurations have better heat transfer/pressure drop ratios. For similar values of pressure drop over a heat exchanger, greater fractions of the total flow are present within the tube bundle; this contributes to better heat transfer.

When considering the higher cross-flow percentages of the double-segmental and disc-and-doughnut configurations, two things have to be mentioned. Firstly, the direction of the flow situated in the cross-flow region is not perpendicular to the tubes (pure cross-flow) which reduces the effectiveness of the heat transfer. Secondly, the heat transfer, as well as sediment transport is favourably influenced by velocity, which, according to Table 21 is highest for the single-segmental configurations.

5.2.7. Steady-state simulation discussion

From the discussion presented on the steady-state simulations, a clear conclusion can be drawn on the selection of configurations for the transient multiphase simulations: velocity distributions are the primary indicators of configuration applicability for sediment transport, while all other results are secondary.

The pressure drop results that have been presented, along with correlations from literature, are in good agreement. The percentage difference between the correlation and the numerical results are negligible - possibly due to the error inherent to the correlation as the present results fall within the error margins. If the heat exchangers are only allowed a limited pressure drop, the double-segmental and disc-and-doughnut configurations are ideal.

When considering bypass flow, the single-segmental configurations have lower-average performance characteristics compared to the other configurations. The maximum values for all configurations are very near the maximum values within the bundle, but one has to take into account that the maximum might fall near the edge of the bundle, which could be seen as ineffective flow (see baffle velocity distributions in Appendix E). The average velocity performance of the single-segmental configurations is the not as good as the small difference between bypass and bundle averages of the double-segmental configurations but the performance is negatively influenced by the detrimental sedimentation transportation characteristics.

The maximum and average baffle-cut velocities are in favour of the Single_60 and Double_60 configurations. The values are consistently higher than both the other configurations' velocities. The performance of the double-segmental and Single_90 configurations have greater consistency when compared to the disc-and-doughnut configurations, but still fall below the performance of the first mentioned configurations.

Distribution of the volume percentage of velocity indicates the single-segmental configurations as the best performing configurations. The large concentration of high-velocity distributions and the small concentration of low-velocity distributions, as compared to the opposite for other configurations, clearly indicate the superiority of the single-segmental configurations. A comparison between configurations of the percentage of velocity situated in the bypass regions reinforces this observation.

Results of fractions that have been tabulated above are in favour of the disc-and-doughnut configurations, the single-segmental configurations being the least favourite. These results are, however, secondary to those of the volume percentages. An increase in mass flow is less important than higher velocities, also relating to downstream sediment transportation.

From the discussion above and the first part of this chapter, one can conclude that the single-segmental configurations are the models which will have the best sediment transport performances. The Single_90 configuration performs slightly poorer than the base case when comparing the higher mid-range velocities and baffle velocity distributions, but still has better performance than other configurations, making it the more favourable configuration for further investigation.

5.3. Single_60 vs. Single_90

A detailed comparison between the Single_60 and Single_90 configurations are presented in this subsection.

5.3.1. High velocity range volume percentage

The higher range velocities of the configurations have been arranged and are tabulated below. The ranges have been split into cells with velocities above 1 m/s, 1.5 m/s and 2 m/s.

	1<V	1<V Main	1.5<V	1.5<V Main	2<V	2<V Main
Single_60	15%	12%	11%	7%	3%	2%
Single_90	15%	10%	8%	5%	1%	1%

Table 24: High velocity volume percentages

The base configuration has better and larger distribution of velocity values throughout the higher ranges in comparison to the Single_90 configuration that has similar performance, but lacks significant concentrations in regions higher than 2 m/s.

Table 24 shows that the increased percentage of high velocity for the Single_90 configuration observed in Table 21 is only situated in a velocity range of 0.5 m/s to 1 m/s. The Single_60 configuration shows improved results for the high velocity region, albeit a negligible difference.

5.3.2. Baffle velocities

Figure 53 to Figure 55 show the velocity distributions on a plane perpendicular to the baffle window flow, parallel to the baffle. The velocity distributions range consistently from 0 m/s to 3 m/s; this is not the maximum for the configurations, but is an intermediate value to enable a straightforward comparison between configurations.

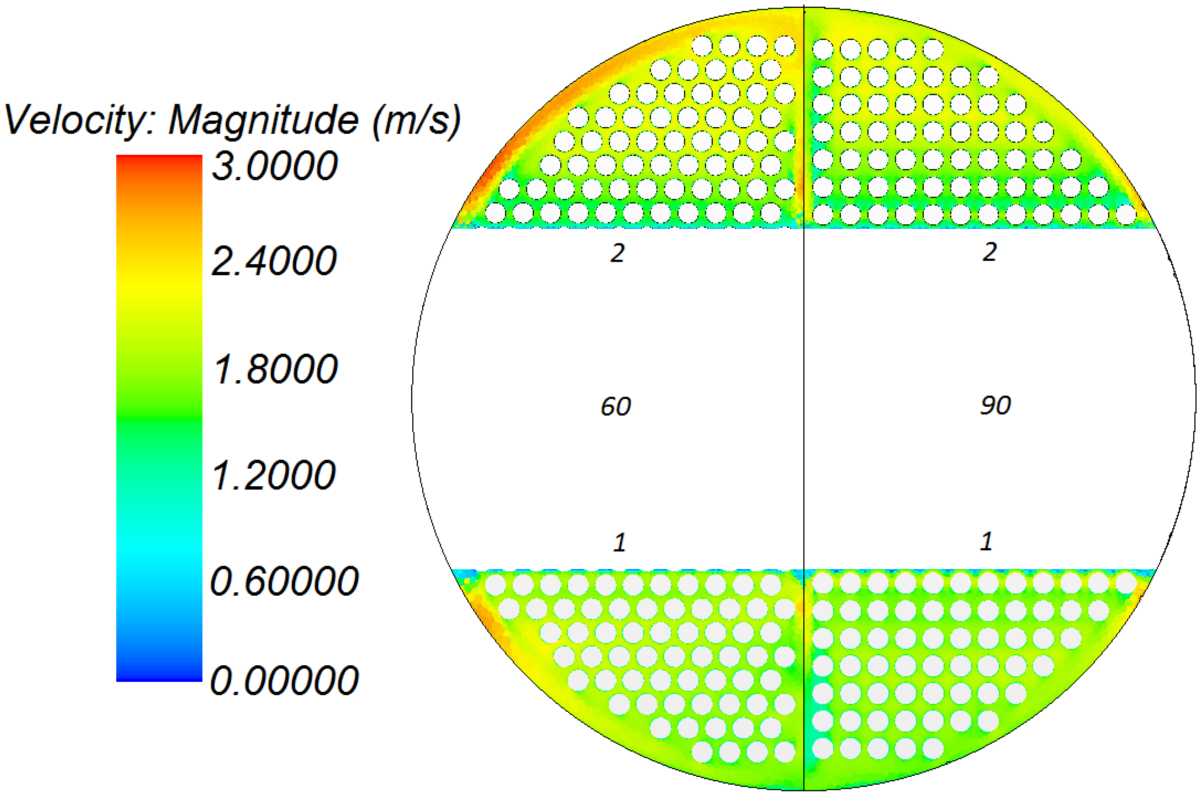

Figure 53: Baffle 1 and 2 velocity distributions for the Single_60 and Single_90 configurations

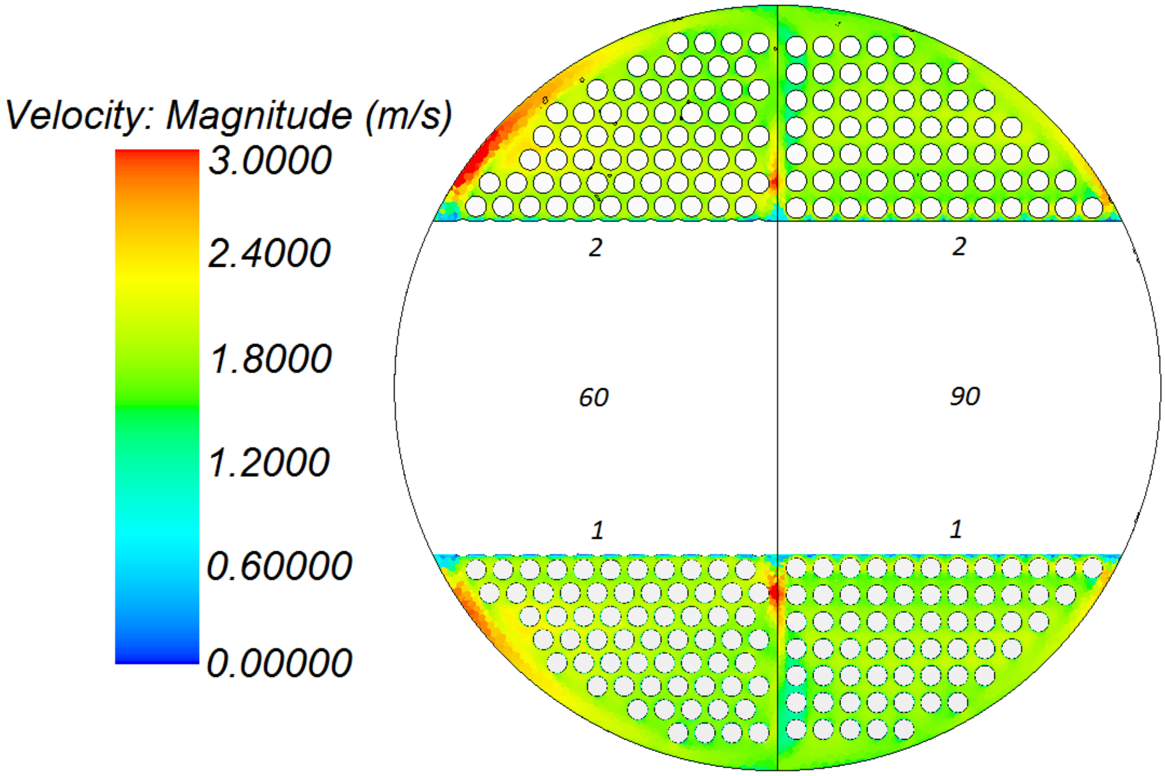

Figure 54: Baffle 3 and 4 velocity distributions for the Single_60 and Single_90 configurations

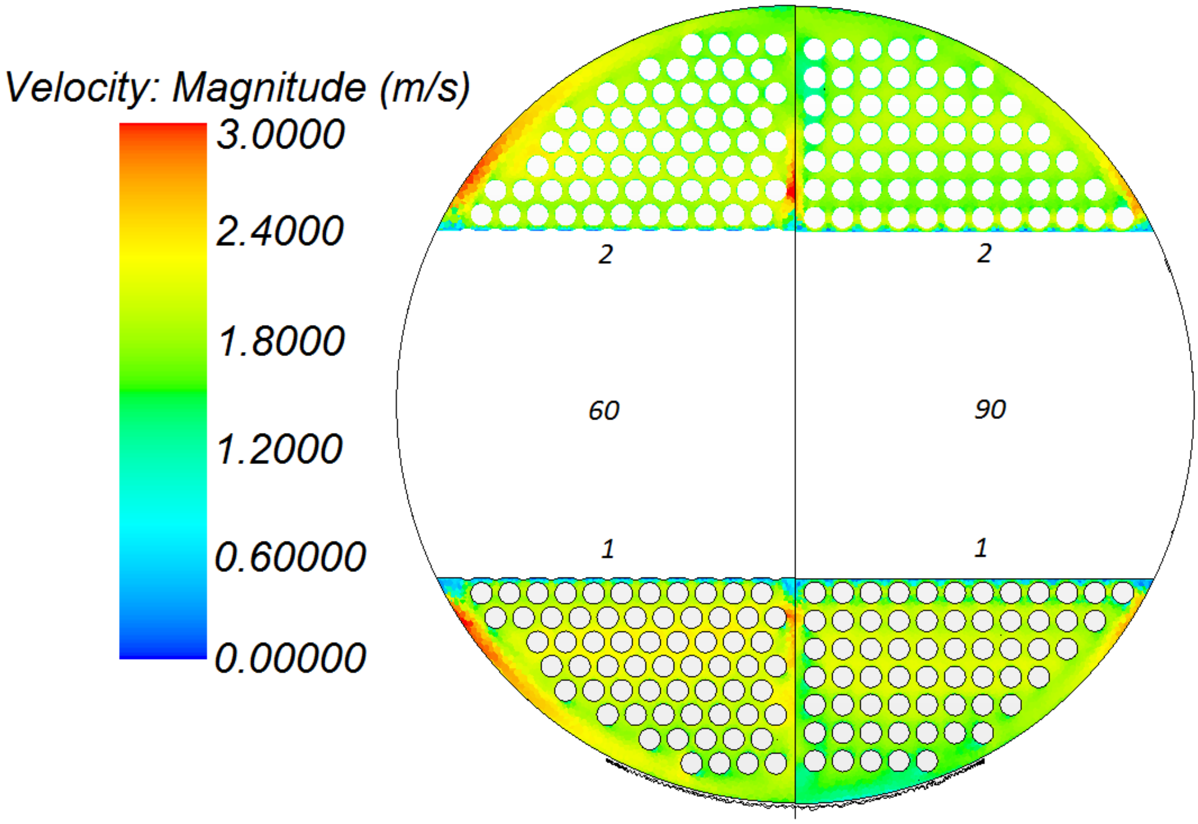

Figure 55: Baffle 5 and 6 velocity distributions for the Single_60 and Single_90 configurations

Figure 53 is the comparison between the first and second baffles (bottom and top respectively). It gives a clear indication of the fluid distribution in the heat exchangers. Comparison of the first baffles shows the flow profiles to be similar to a large extent. There is a slight tendency of the Single_60 configuration to have a larger area with higher velocities, evidenced by Table 19.

The second baffles start to show the influence of the bundle as the flow develops. The greater resistance of the triangular tube array starts to show in the bundle bypass flow (yellow region at the top), and lacking within the bundle. The square tube configuration does not show this occurrence as notably. The prominence of these flow characteristics continues to develop in Figure 54 and Figure 55.

The figures above show significant high velocity distributions in the bundle-shell bypass region of the Single_60 configuration. From these results, it can be expected that the Single_60 configuration will have better sediment transport and heat transfer characteristics because of these higher velocity regions.

5.3.3. Symmetry plane flow distribution

The shell-side flow distributions on the symmetry planes are once again shown in Figure 56 and Figure 57 for the single-segmental configurations.

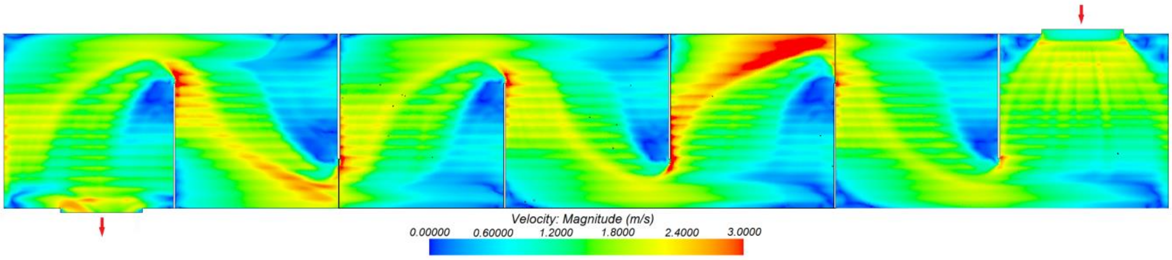

Figure 56: Single_60 flow distribution on the symmetry plane

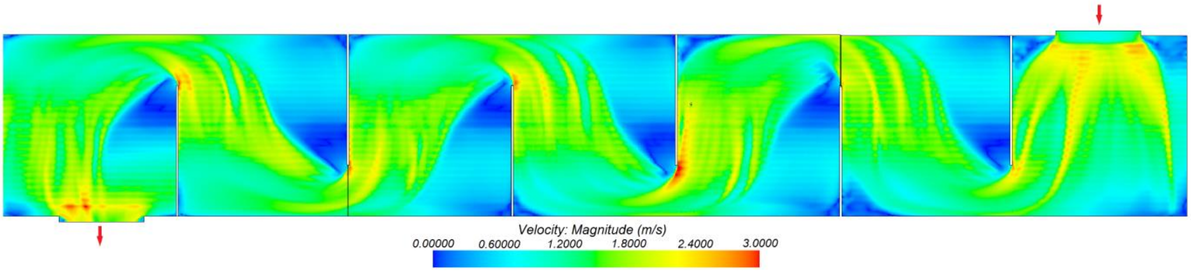

Figure 57: Single_90 flow distribution on the symmetry plane

The Single_60 configuration is shown to have higher velocities throughout the heat exchanger with comparatively smaller recirculation regions around the baffles. Taking the velocity distribution in Table 22 and the comparison between average baffle velocities into account, the base configuration performs slightly better. The symmetry plane is, however, coplanar with the pass-partition bypass stream which, for the Single_60 configuration, has larger velocity differences between bundle and bypass, indicating that the results could be deceiving.

The red streak seen in the third compartment of the Single_60 configuration is attributed to the flow field not being fully developed resulting in areas of minor discrepancies stemming from the inlet. The results of the simulation were fully converged to the indicated level of convergence, as discussed in Chapter 4.1.6 thus the indicated discrepancy does not stem from convergence issues or from inaccuracies due to mesh generation.

From Table 23, the mass flow results indicate that in the Single_60 configuration, 2% more flow is situated in the pass-partition plane, whilst there is 7% more flow in cross-flow in the Single_90 configuration. Taking the results of Table 21 into account, there is also a greater percentage of high velocity cross-flow in the Single_90 configuration, which could falsely indicate improved heat transfer, but this higher velocity flow is situated in the planes between tubes and does not encounter as much heat transfer surface area as in the Single_60 configuration.

It will have to be observed experimentally or numerically which configuration has the best performance with regard to the single-segmental configurations' sedimentation characteristics. It can be argued that the Single_90 configuration will have the least amount of sedimentation inside of the bundle, sustaining the heat transfer surface area for longer because of the high cross-flow velocities. On the other hand, the Single_60 configuration might be more sustainable in the long run, because of an improved velocity distribution; because of the high bypass velocities, the fluid that acts to remove sediment in the bundle will be swept away by the bypass flows.

A final remark on the steady-state modelling of the different configurations has to be made. It will have to be studied if the method of splitting a heat exchanger into three sections has proved successful. There could be issues regarding the rearward flow of information over the inlet-outlet boundaries of the segments, conveyance is only in the direction of flow. The influence on the observed flow patterns will have to be investigated by studying the flow and pressure drop characteristics of simplified models; one segmented as in the present study, one whole (all seven compartments combined).

5.3.4. Appendices

Appendices B to I can be found on the CD-ROM disc accompanying the present study. A brief description on the contents of each of the appendices follows.

Appendix D presents the cross-flow vector plots, spaced 200 mm apart and situated in the second last compartment of each heat exchanger. Because the planes are consecutive, it offers a representation of the inter-tube flow profiles.

Appendix E presents the baffle-cut velocity distributions for all of the configurations. These images are similar to Figure 53 to Figure 55 and give the reader an indication of the velocity distribution and magnitude within the longitudinal flow regions of the heat exchangers.

The visual results in Appendix F are the symmetry plane vector plots and are similar to the magnitude of the velocity distribution in Figure 43 through Figure 48. These images facilitate a better understanding of the flow profiles and directions within the compartments. The information contained therein is especially valuable for understanding the flow in the recirculation zones.

The streamlines depicted in Appendix G give an overall indication of the flow profiles that are prevalent in the shell side. The lines are generated at the inlet of each of the 18 simulations, equally spaced and follow the path a fluid element or particle would follow. The lines also give an indication of the velocity of the surrounding fluid by means of the colour distribution on their surfaces.

The representations of velocity concentrations are available in Appendix H. There are four images for each of the 18 simulations for velocity distributions above 0.5 m/s, 1 m/s, 1.5 m/s and 2 m/s. The images were once again generated by using the threshold function incorporated in STAR-CCM+. These images give an isometric view of where certain ranges of the velocity are situated.

The magnitude of the velocity distribution presented in Figure 43 through Figure 48 is presented in Appendix I as single images generated from each of the 18 simulations.

5.4. Transient multiphase simulations

The results of the transient multiphase simulations are presented in this section. Visual representations of the sediment concentrations are depicted at various time steps. The following images have been adjusted to allow for improved physical presentation. The unadjusted images are available in Appendices J and K.

5.4.1. Symmetry plane sediment volume fraction

Images of the sediment flow path on the symmetry plane are presented in Figure 58 to Figure 67 for both the single-segmental configurations, generated at the end of each time step, unable to be modified. It is unfortunate that the scales for the Single_60 and Single_90 do not match; they are, however, still comparable.

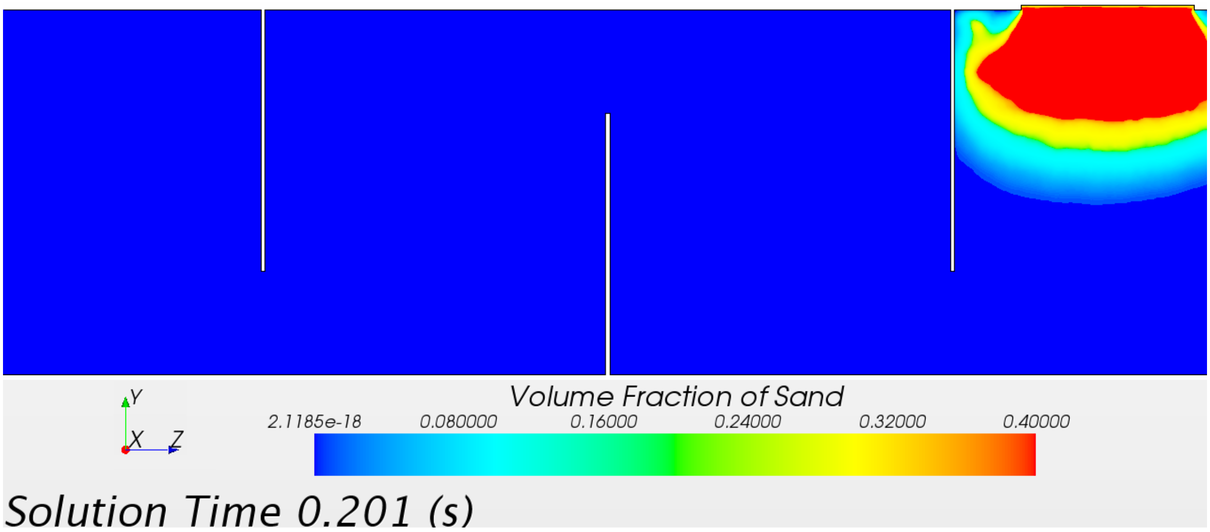

Figure 58: Sediment fraction of Single_60 configuration at solution time = 0.201 seconds

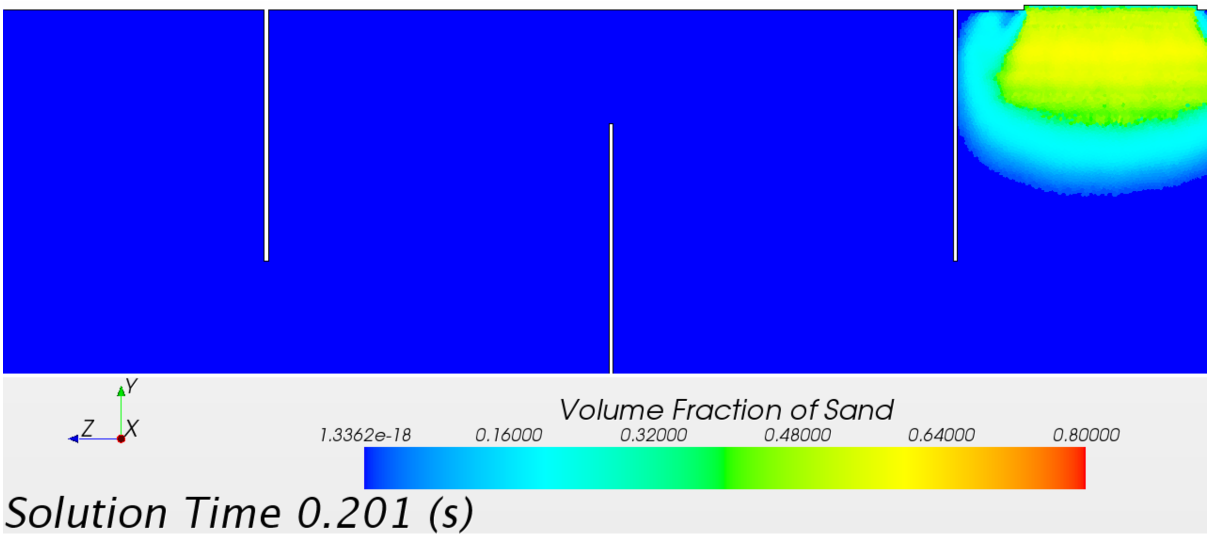

Figure 59: Sediment fraction of Single_90 configuration at solution time = 0.201 seconds

The sediment distribution at 0.201 seconds shows that the flows for both configurations have the same tendencies and have propagated similarly.

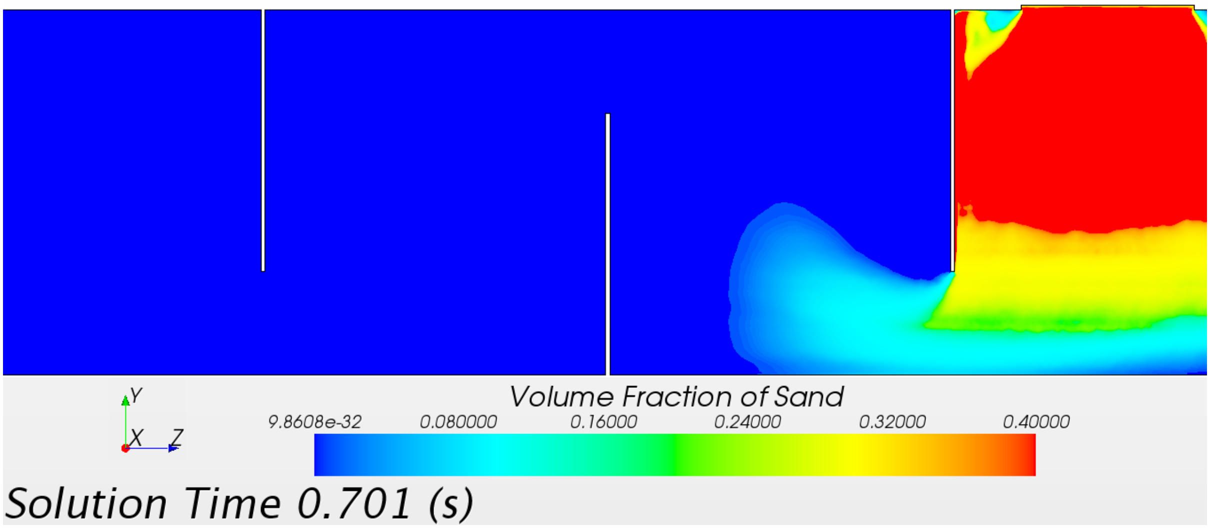

Figure 60: Sediment fraction of Single_60 configuration at solution time = 0.701 seconds

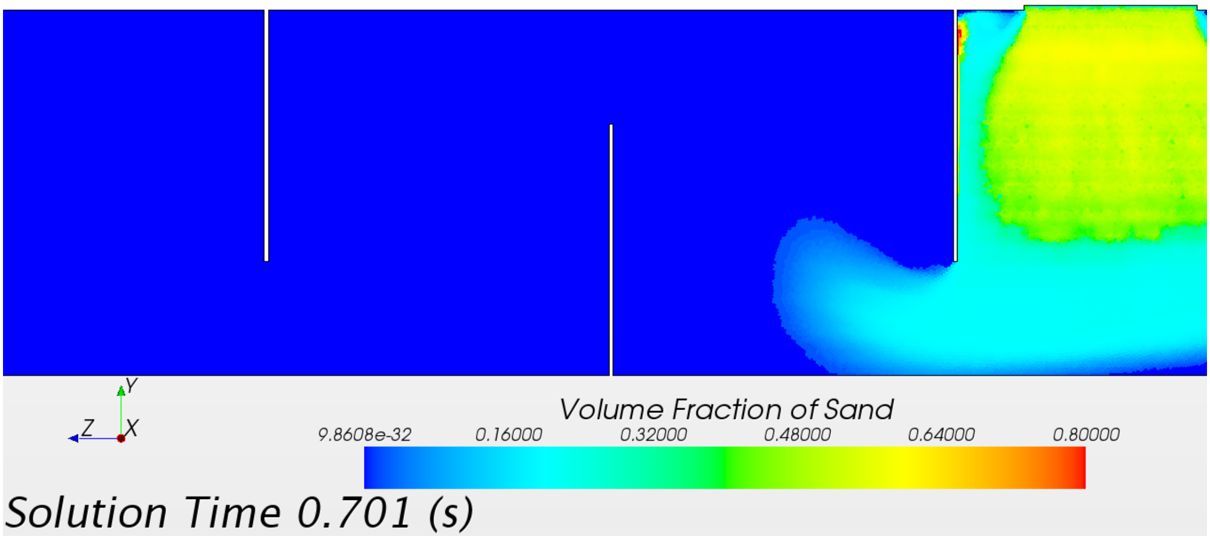

Figure 61: Sediment fraction of Single_90 configuration at solution time = 0.701 seconds

At solution time 0.701 seconds, the propagation is once again at the same position. A deposition of sediment can be seen beside the inlet for both configurations.

As the flow exits the inlet pipe, the peripheral part of the inlet stream diverges because of a combination of the resistance presented by the bundle and the shear forces experienced when interacting with the slower moving/stationary fluid close to the inlet periphery. The flow is similar to the free shear, round jet flow.

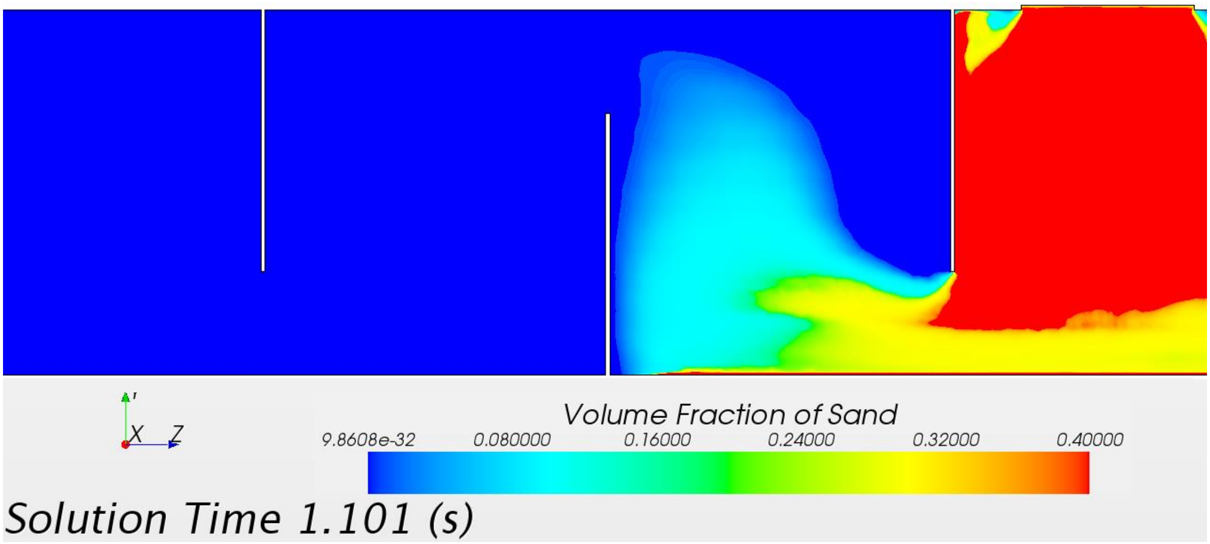

Figure 62: Sediment fraction of Single_60 configuration at solution time = 1.101 seconds

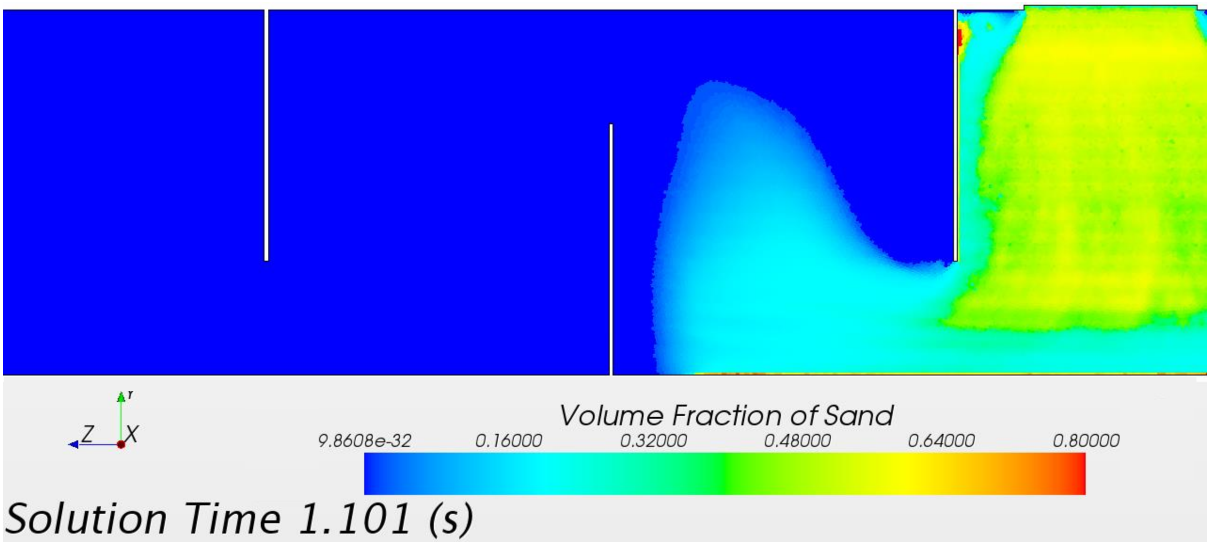

Figure 63: Sediment fraction of Single_90 configuration at solution time = 1.101 seconds

At time step 1.101 seconds, some difference between the configurations are visible, although slight. In the Single_60 configuration, a higher concentration of sediment has been transported further downstream. Taking into consideration that the depicted flow is coplanar with the pass-partition stream, the enhanced propagation indicates that flow is more likely to transport the sediment by means of the bypass streams and possibly not through the bundle itself. This can also be seen in Table 18, where the average velocity of the pass-partition stream is higher for the Single_60 configuration.

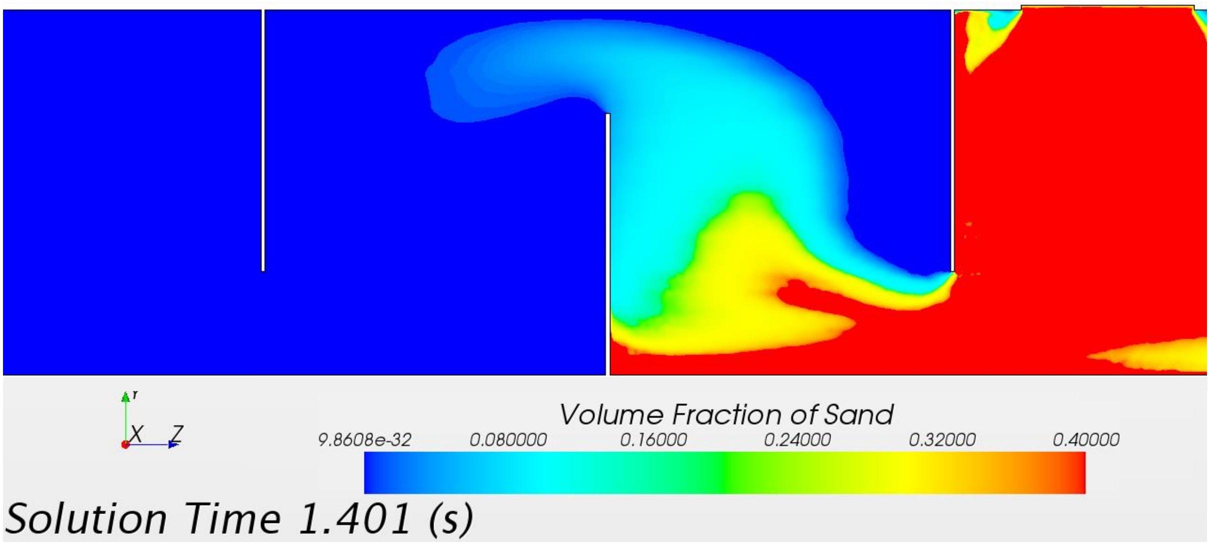

Figure 64: Sediment fraction of Single_60 configuration at solution time = 1.401 seconds

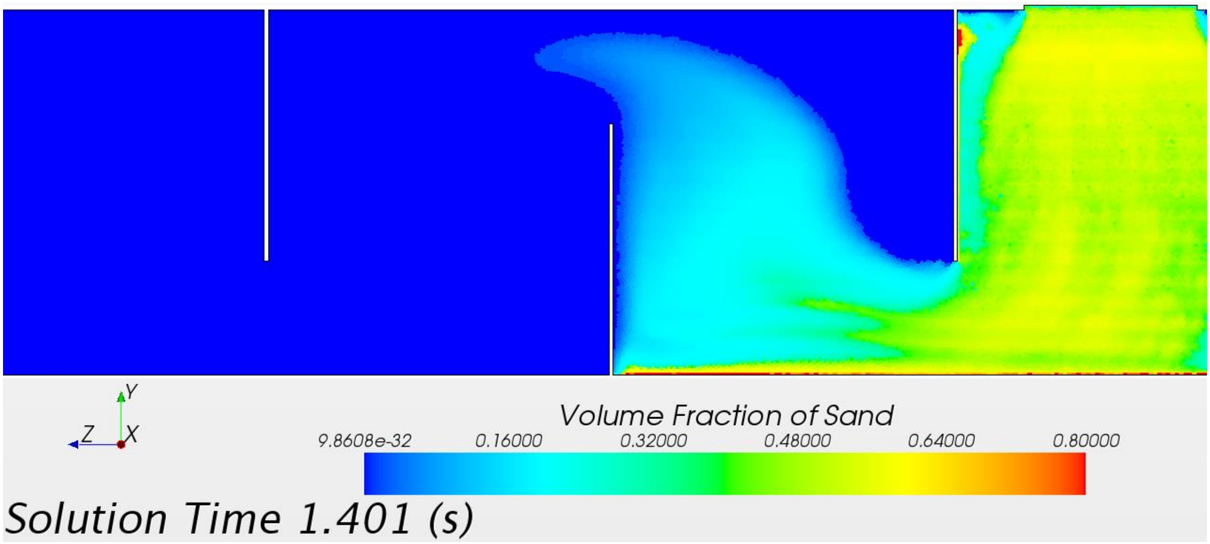

Figure 65: Sediment fraction of Single_90 configuration at solution time = 1.401 seconds

At time 1.401 seconds, a clear performance difference between the configurations is established. Although the colour bar discrepancy makes it difficult to compare the configurations directly, it is evident that the Single_60 configuration experiences deposition sooner. Comparing the regions of concentration that are higher than 40%, it is clear that the Single_60 configuration has a larger deposition area. It can consequently be assumed that higher concentrations of sediment will be present within this region, indicating that the sediment transportation capabilities of the Single_90 configuration are better.

The final images for the simulations (Figure 66 and Figure 67) show trends that are similar to previous images and discussions. It is interesting to note that the velocity into the second compartment is insufficient for sediment transport, resulting in the deposition of sediment in the bottom left corner of the heat exchanger, which is in line with expert opinion (Da Veiga, 2012).

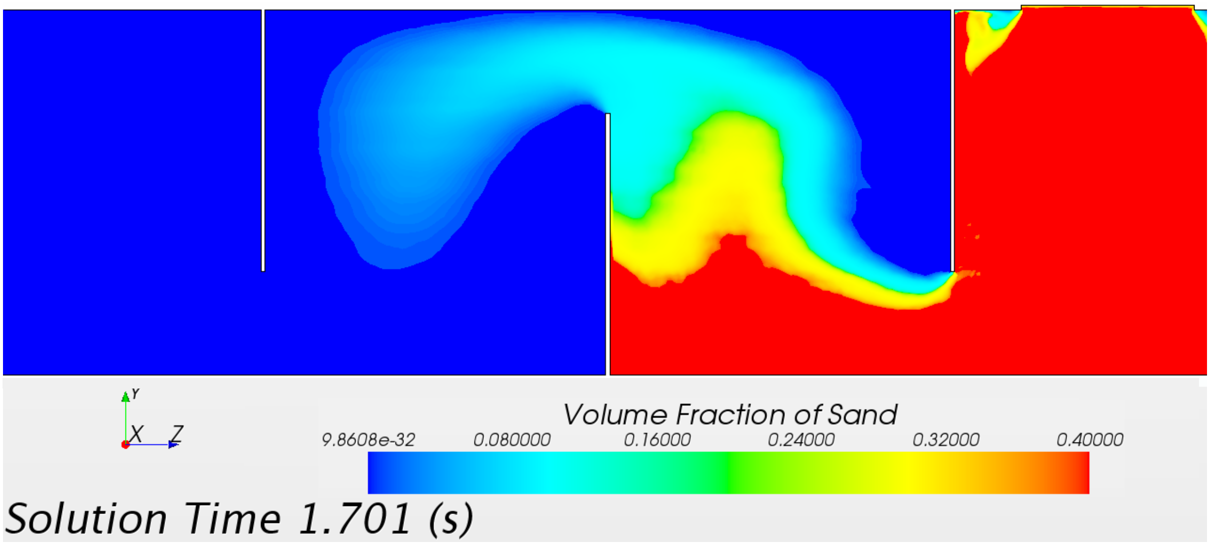

Figure 66: Sediment fraction of Single_60 configuration at solution time = 1.701 seconds

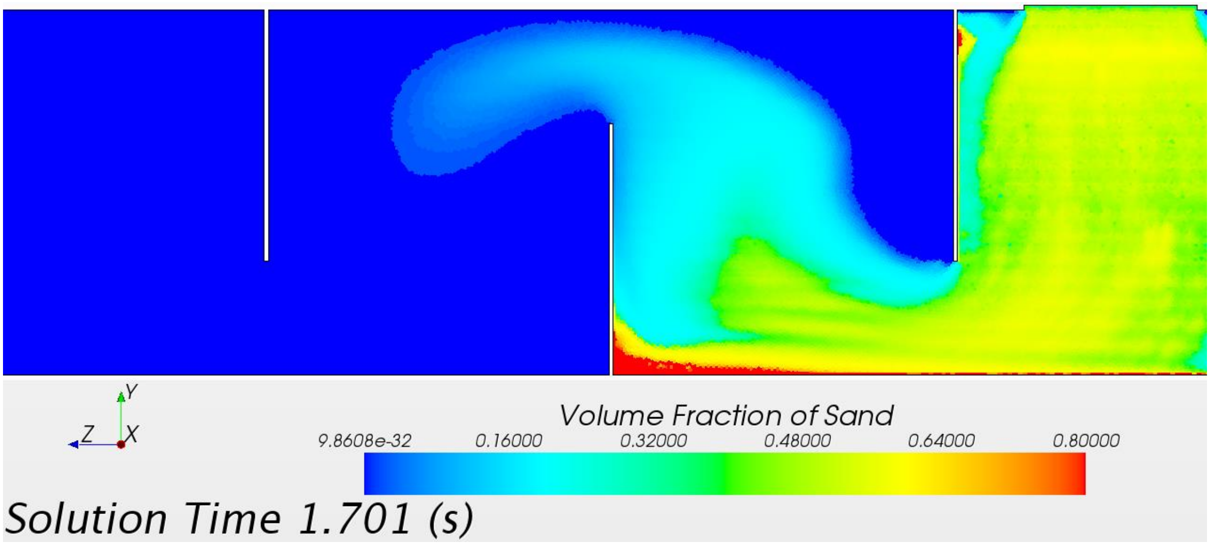

Figure 67: Sediment fraction of Single_90 configuration at solution time = 1.701 seconds

Contrary to this opinion, the sediment deposition in the bottom right corner of the first compartment is trivial in comparison to the bottom left corner of the second compartment. It is attributed to the bundle-shell bypass flow that transports the sediment into the free stream or against the second baffle. This would, however, not be the case if the influence of sealer strips were taken into account.

Had the simulation been running for a time period longer than 2-3 months, it would be expected that the sediment deposition in the corner of the second compartment would increase. It would continue up to a point where the reduction in flow area would be sufficient to allow for a state of equilibrium between deposition and erosion. In Figure 67 it can be seen that although there is deposition in the second compartment, some sediment is transported to the third compartment. Once this equilibrium state has been reached, the bulk of the deposition would occur downstream of the second baffle in the recirculation zone. This occurrence will continue until all the compartments are fouled, up to a point where the flow is reduced too much to allow for further deposition.

5.4.2. Cross-sectional sediment concentration

The concentration of sediment through a plane behind the first baffle at certain time steps has been measured visually. The results for the Single_60 and Single_90 are displayed in Figure 68 to Figure 73. By analysing the data from Figure 58 to Figure 63 and in Appendix J, it was observed that the sediment will cross the plane at time 0.401 seconds. The images below, however, are for time step 0.801 to 1.101 seconds with 0.1 intervals, the Single_60 configuration on the left.

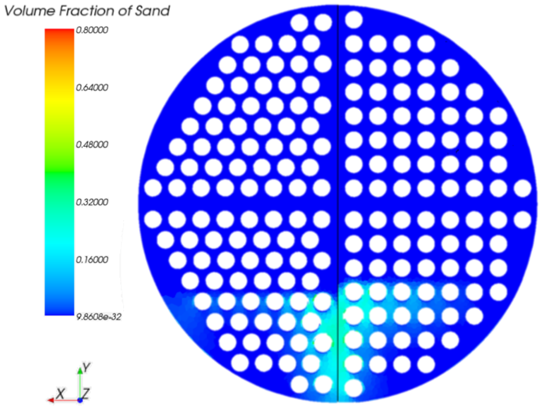

Figure 68: Sediment concentration behind baffle 1 at time step 0.801

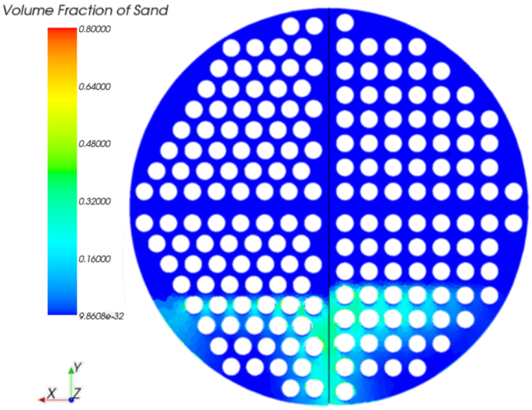

Figure 69: Sediment concentration behind baffle 1 at time step 0.901

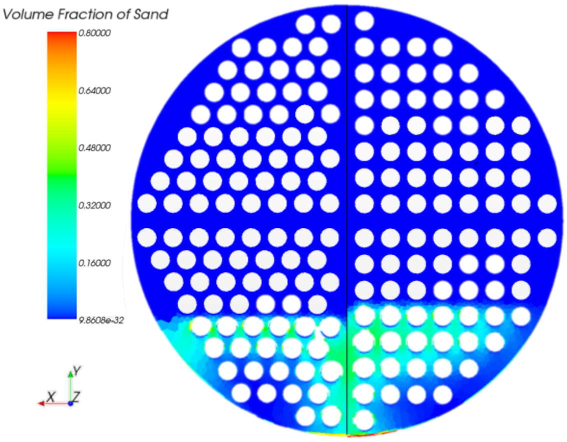

Figure 70: Sediment concentration behind baffle 1 at time step 1.001

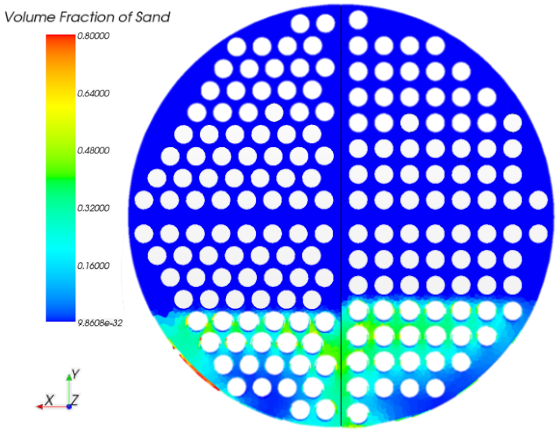

Figure 71: Sediment concentration behind baffle 1 at time step 1.101

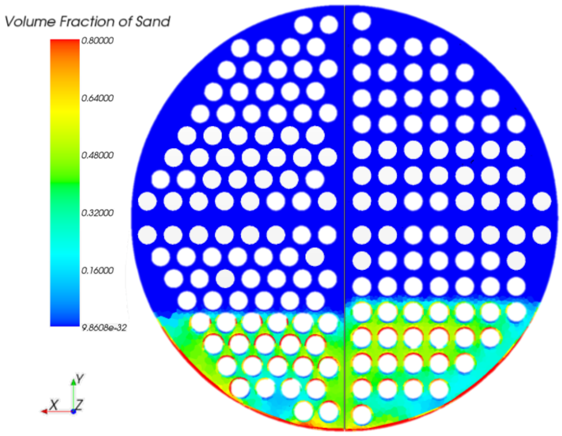

Figure 72: Sediment concentration behind baffle 1 at time step 1.401

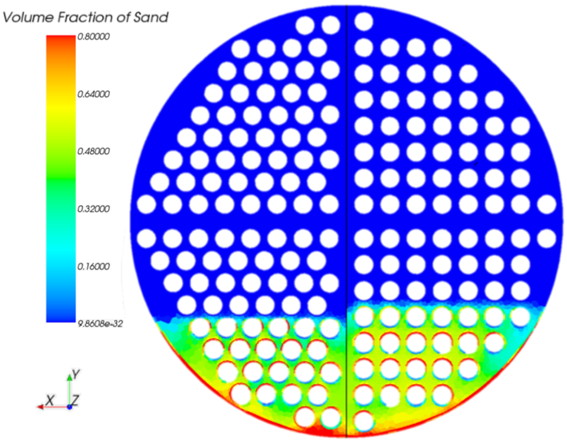

Figure 73: Sediment concentration behind baffle 1 at time step 1.701

Three important aspects of Figure 68 to Figure 73 are highlighted: the first is the concentration of the sediment on the shell at time steps 1.101 and 1.701 seconds (Figure 71 and Figure 73). The Single_60 concentration is clearly shown to have larger concentration, higher up on the shell. Secondly, the flow of sediment in the window zone of the Single_90 configuration has a higher and better distributed cross-flow concentration. Lastly, the Single_60 configuration has higher sediment concentrations in the bundle-shell bypass flow areas and is shown to have a large build up of sediment around the tubes closest to the shell. It also has to be noted that the Single_90 has a higher concentration of sediment in the 60% range that is close to the shell.

The following conclusions can be drawn: the flow through the first compartment of the Single_90 bundle is faster, resulting in better transportation of higher quantities of sediment downstream. This is a positive result, but does not necessarily mean that all the sediment will exit through the heat exchanger outlet. If one observes the figures of streamlines in Appendix G, it can be seen that for the Single_90 configuration, a lower percentage of the lines exits the heat exchanger in comparison to the Single_60 configuration.

The influence of the higher velocity bypass streams is clearly noted to increase sedimentation on the tubes as well as the shell. Although the Single_90 configuration experiences higher deposition rates on the tubes earlier in the simulation, the possibility still exists that sediment could possibly be transported downstream. The expectation would be that deposits on the shell, as seen in the Single_60 configuration, are more detrimental than sedimentation on the tubes.

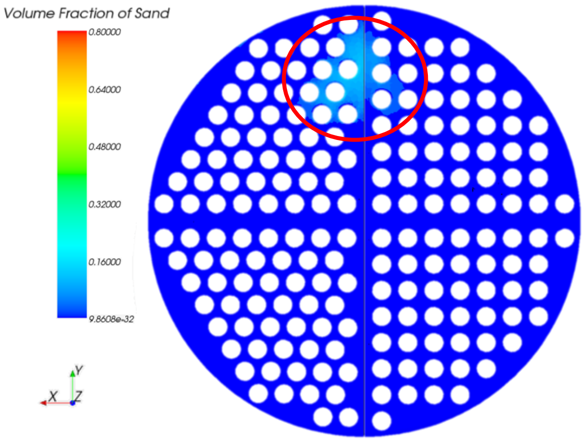

Figure 74: Sediment concentration behind baffle 2 at time 1.401

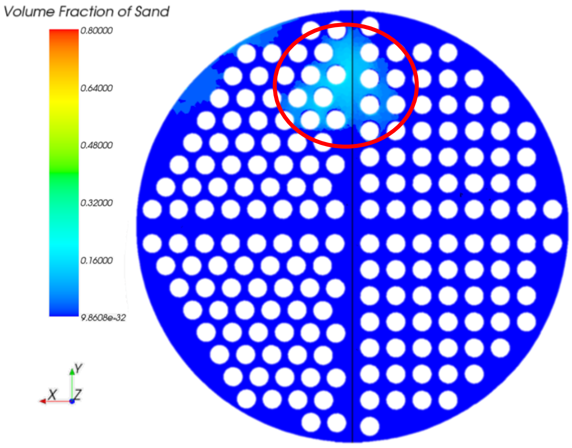

Figure 75: Sediment concentration behind baffle 2 at time 1.501

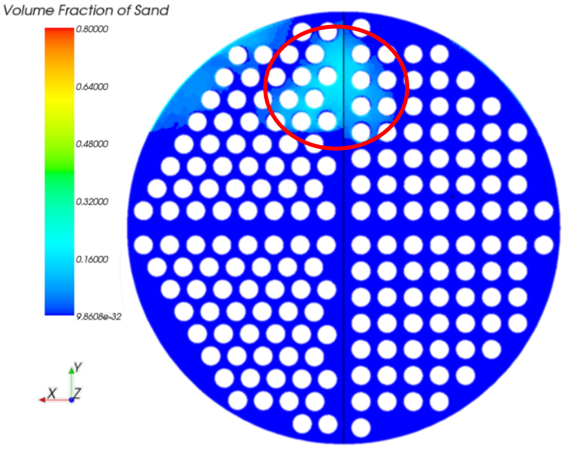

Figure 76: Sediment concentration behind baffle 2 at time 1.601

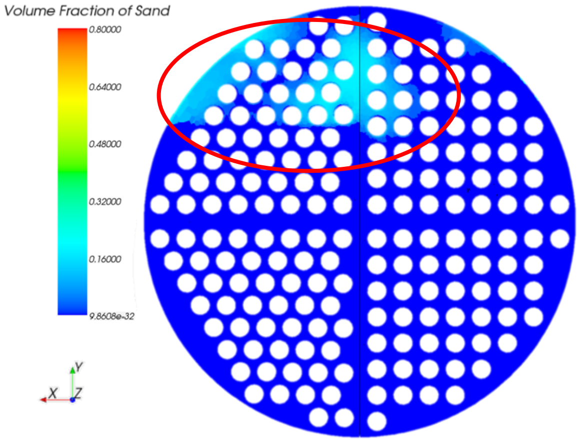

Figure 77: Sediment concentration behind baffle 2 at time 1.701

Figure 74 to Figure 77 is a representation of the sediment concentration behind the second baffle. It gives an indication of the transport characteristics of sediment through the bundle. At time 1.401 seconds, it can be seen that the sediment in the Single_60 configuration has crossed the plane. It is interesting to note that the profile of the concentration in both configurations is similar, that is the sediment is transported by the bypass streams and no longer through the bundle for the Single_90 configuration. It is better shown in Figure 78 and Figure 79, although here, it is 0.2 seconds later.

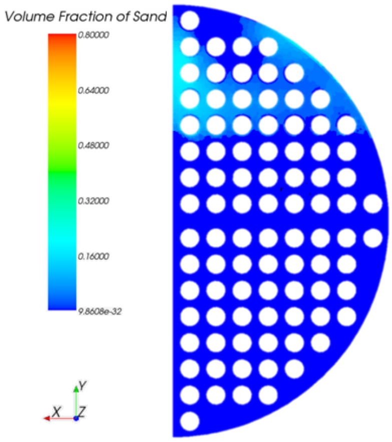

Figure 78: Sedimentation of Single_90 configuration behind baffle 2 at time 1.801

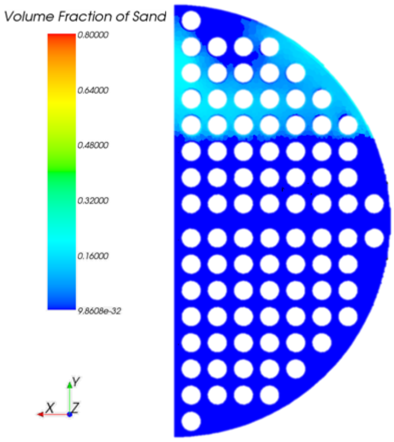

Figure 79: Sedimentation of Single_90 configuration behind baffle 2 at time 1.901

5.4.3. Appendices

Two final appendices for the transient multi-phase results are available on the accompanying CD-ROM. Appendix J depicts the symmetry plane sediment progress at different time steps, similar to Figure 68 through Figure 73. The remaining, unedited images of Figure 74 to Figure 79 for the time steps omitted are presented in Appendix K.

5.4.4. Transient multiphase simulation discussion

From the results that have been presented on the transient multiphase simulations, it is probable that the Single_60 has higher pressure drop due to the higher velocities that has been observed. This is evident in the images that are shown on the progress of the concentration profiles, which leads one to believe that the base case might be the best configuration for sediment transport.

This seems to be in contrast with the sedimentation profiles that have been observed in Figure 72 and Figure 73, where the Single_60 configuration has higher deposit concentrations. However, two things need to be considered: Firstly, the sediment concentration in the window zone is on average much higher for the Single_90 configuration. Secondly, the images that are portrayed still fall within the first two seconds of simulation and the sedimentation rates and trends that have already been observed will tend to vary as the simulation progresses because of the flow area reduction.

The fact that the sediment reaches the plane behind the second baffle of the Single_60 configuration earlier than the Single_90 configuration is an important aspect to take into consideration. This indicates that the velocity at which sediment is transported is lower for the latter configuration, indicating that the same quantity of sediment occupies a smaller volume.

From the discussion and configuration comparison above, it can be deduced that the base case is the best configuration for sediment suspension and transport.

5.5. Conclusion

The results of the study have been presented and discussed, clearly indicating that the performance of the Single_60 configuration is the best. A thorough investigation into the most suitable configuration was initiated by investigating the mesh requirement and by verifying to which extent the study could be completed successfully.

A detailed discussion on the six configurations was presented, discussing and highlighting the hydraulic characteristics of the models. The two single-segmental configurations were singled out for a more detailed investigation, concluding that the transient multiphase simulations were successful in identifying the base case as the best configuration for sediment transport.